

1 **Moist static energy budget analysis of tropical cyclone formation and**
2 **intensification in high-resolution climate models**

3 Allison A. Wing*

4 *Department of Earth, Ocean and Atmospheric Science, Florida State University, Tallahassee,*
5 *Florida*

6 Suzana J. Camargo

7 *Lamont-Doherty Earth Observatory, Columbia University, Palisades, New York*

8 Adam H. Sobel

9 *Department of Applied Physics and Applied Mathematics and Lamont-Doherty Earth*
10 *Observatory, Columbia University, New York, New York*

11 Daehyun Kim

12 *Department of Atmospheric Sciences, University of Washington, Seattle, Washington*

13 Yumin Moon

14 *Department of Atmospheric Sciences, University of Washington, Seattle, Washington*

15 Hiroyuki Murakami

16 *NOAA/Geophysical Fluid Dynamics Laboratory and Princeton University, Princeton, New Jersey*

17 Kevin A. Reed

18 *School of Marine and Atmospheric Sciences, Stony Brook University, Stony Brook, New York*

19 Gabriel A. Vecchi

20 *Princeton University, Princeton, New Jersey*

21 Michael F. Wehner

22 *Lawrence Berkeley National Laboratory, Berkeley, California*

23 Colin Zarzycki

24 *National Center for Atmospheric Research, Boulder, Colorado*

25 Ming Zhao

26 *NOAA/Geophysical Fluid Dynamics Laboratory, Princeton, New Jersey*

27 *Corresponding author address: Department of Earth, Ocean and Atmospheric Science, Florida

28 State University, P.O. Box 3064520, Tallahassee, FL 032306.

29 E-mail: awing@fsu.edu

ABSTRACT

30 Tropical cyclogenesis and intensification processes are explored in six high-
31 resolution climate models. The analysis framework employs process-oriented
32 diagnostics that focus on how convection, moisture, clouds and related pro-
33 cesses are coupled. These diagnostics include budgets of column moist static
34 energy and the spatial variance of column moist static energy. The latter al-
35 lows for the quantification of the different feedback processes responsible for
36 the amplification of moist static energy anomalies associated with the organi-
37 zation of convection and cyclogenesis, including surface flux feedbacks and
38 cloud-radiative feedbacks. Tropical cyclones (TCs) are tracked in the climate
39 model simulations and the analysis is applied along the individual tracks and
40 composited over many TCs. Two methods of compositing are employed: a
41 composite over all TC snapshots in a given intensity range, and a composite
42 over all TC snapshots at the same stage in the TC life cycle (same time rela-
43 tive to the time of lifetime maximum intensity for each storm). The radiative
44 feedback contributes to TC development in all models, especially in storms
45 of weaker intensity or earlier stages of development. Notably, the surface flux
46 feedback is stronger in models that simulate more intense TCs. This indicates
47 that the representation of the interaction between spatially varying surface
48 fluxes and the developing TC is responsible for at least part of the inter-model
49 spread in TC simulation.

50 **1. Introduction**

51 The study of tropical cyclones (TCs) in climate models has long been difficult because of the
52 conflict between the high resolution necessary to accurately simulate TCs and the need to perform
53 long, global simulations. In recent years, however, enormous progress has been made in the ability
54 of general circulation models (GCMs) to simulate TCs from subseasonal to seasonal and longer
55 time scales (Camargo and Wing 2016). Global forecast models have become a more reliable
56 source of tropical cyclone (TC) genesis guidance (e.g., Halperin et al. 2016) while climate models
57 have improved such that they can reproduce the TC climatology with some fidelity (e.g., Zhao
58 et al. 2009; Wehner et al. 2014) and exhibit some skill in seasonal forecasting (Zhang et al. 2016;
59 Vecchi et al. 2014; Murakami et al. 2015, 2016; Vitart et al. 2010; Chen and Lin 2011, 2013).
60 This is largely a result of algorithmic and computational advances that have allowed for the use of
61 high horizontal resolutions that substantially improve the simulation of TC climatology, structure,
62 and intensity. However, biases remain. For example, low-resolution GCMs tend to simulate too
63 few TCs globally (Camargo 2013), and even 50 km high-resolution models are generally not
64 able to simulate the most intense storms (Shaevitz et al. 2014). While decreasing the model grid
65 spacing can improve the low intensity bias (Manganello et al. 2012; Wehner et al. 2014; Murakami
66 et al. 2015), it does not do so uniformly (Roberts et al. 2015), and even in models with the same
67 resolution, there can be a substantial difference in their ability to simulate TCs (Shaevitz et al.
68 2014). This suggests that resolution is not the only factor controlling model simulation of TCs. In
69 particular, TCs are tightly coupled to clouds and convection, so TC frequency, intensity, structure,
70 and interannual variability are strongly sensitive to the details of convective parameterizations
71 (e.g., Reed and Jablonowski 2011; Murakami et al. 2012; Zhao et al. 2012; Kim et al. 2012; Duvel
72 et al. 2017). These biases contribute to uncertainty regarding future projections of TC activity

73 (Walsh and coauthors 2016), as such projections depend on the the ability of GCMs to reliably
74 capture the features of TC activity.

75 Our objective is to develop process-oriented diagnostics to identify model characteristics that are
76 responsible for proper simulation of TCs and that will explain the inter-model spread in TC fre-
77 quency and intensity distributions. These diagnostics go beyond simply quantifying the simulated
78 TC activity and focus on how simulated TCs respond to their environments, rather than how the
79 large-scale environment itself is simulated across different models. Our study builds on the work
80 of Kim et al. (2018), which introduced a suite of diagnostics that provided deeper insights into
81 the representation of physical processes that are responsible for the simulation of TCs in GCMs.
82 The Kim et al. (2018) diagnostics consist of azimuthal averages of dynamic and thermodynamic
83 fields around the storm center and identify physical processes related to the interaction between
84 convection, moisture, and circulation that can lead to inter-model differences in simulated TCs.
85 Of the three models examined, they found that the one with the most intense storms had the most
86 precipitation near the composite TC center, the strongest sensitivity of convection to moisture,
87 and the strongest contrast in relative humidity and surface latent heat flux between the inner and
88 outer region of the composite TCs. These results indicate the importance of moisture-convection
89 coupling and feedbacks between the surface latent heat flux and convection. Here, we develop
90 and apply an additional, related set of diagnostics to further analyze the role of these and other
91 processes in simulated TCs, in six high-resolution climate models.

92 The paper is organized as follows. We provide a brief description of the six high-resolution
93 models used in this study in Section 2 and describe our diagnostics and analysis methodology in
94 Section 3. The application of these diagnostics to the six models will be described in Section 4,
95 with a discussion of their implications in Section 5. We provide a summary of the results and
96 conclusions in Section 6.

97 **2. Model Simulations**

98 *a. Models*

99 We explore TC genesis and intensification processes in six high-resolution climate model long-
100 term (> 20 year) historical simulations (Table 1). While long-term simulations were performed,
101 we only have high-frequency (six-hourly) output available for a subset of several years, on which
102 we focus our analysis. The TC statistics in those years are representative of the model climatology.
103 Several of these simulations were also examined in complementary studies by Kim et al. (2018)
104 and Moon et al. (2018). This six-member model ensemble is an “ensemble of opportunity” based
105 on available simulations, rather than a coordinated intercomparison.

106 Three of the models were developed at the Geophysical Fluid Dynamics Laboratory (GFDL)
107 - Atmosphere Model version 2.5 (AM2.5; Delworth et al. 2012), High Resolution Atmospheric
108 Model (HiRAM; Zhao et al. 2009), and Forecast-Oriented Low Ocean Resolution (FLOR; Vecchi
109 et al. 2014) version of Coupled Model 2.5 (CM2.5; Delworth et al. 2012). AM2.5 and HiRAM
110 are atmosphere-only simulations forced with observed sea surface temperatures from HadISST1.1
111 (Rayner et al. 2003), while FLOR is a coupled simulation in which SSTs are calculated interac-
112 tively by its oceanic component and nudged toward the observed SSTs with a 5-day nudging time
113 scale. This ensures the model mean state remains close to that observed. The ocean component
114 of FLOR has $1^\circ \times 1^\circ$ horizontal resolution, zooming to $1/3^\circ$ meridional spacing near the equator
115 with 50 vertical levels, and an ocean-atmosphere coupling interval of 1 hour. The atmosphere-
116 component of FLOR is AM2.5. All three GFDL models are run with 50 km horizontal resolution
117 and 32 vertical levels in the atmosphere. All three models use the same finite volume dynamical
118 core on a cubed-sphere grid (Putman and Lin 2007), with the same divergence damping coeffi-
119 cient (Zhao et al. 2012), the same time steps, and the same physics-dynamics coupling interval

120 (the gravity wave, advective, and physics time steps are 200, 600, and 1200 s, respectively, and
121 the radiation is called every 3 hours). AM2.5 and FLOR use the same Relaxed Arakawa-Schubert
122 convection scheme (Moorthi and Suarez 1992), while HiRAM uses a version of the Bretherton
123 et al. (2004) shallow convection scheme, modified to simulate both deep and shallow convection
124 (Zhao et al. 2012); all other physics packages are the same (GFDL Global Atmospheric Model De-
125 velopment Team 2004). Therefore, AM2.5 and FLOR differ only in that FLOR is coupled while
126 AM2.5 is atmosphere-only, and AM2.5 and HiRAM differ only in their convection schemes.

127 Two of the additional atmosphere-only models we analyze are versions of the National Center for
128 Atmospheric Research (NCAR)/Department of Energy (DOE) Community Atmosphere Model,
129 version 5 (CAM5; Neale et al. 2012) with both the spectral element (CAM-SE; Dennis et al.
130 2012) and the finite volume (CAM-FV; Lin and Rood 1996, 1997) dynamical cores. CAM-SE
131 is configured with the variable-resolution option (Zarzycki et al. 2014), with 0.25° grid spacing
132 over the North Atlantic and 1° grid spacing elsewhere as in Zarzycki et al. (2017). The raw
133 data are remapped to a globally-uniform 0.25° latitude-longitude grid, although we restrict our
134 analysis to the North Atlantic where the native resolution is highest. CAM-FV is configured with
135 global 0.25° grid similar to the work of Wehner et al. (2014). CAM5 utilizes 30 vertical levels
136 with a model top of approximately 2 hPa. Both CAM-SE and CAM-FV use similar versions of
137 the CAM5 physics parameterizations, including the same deep (Zhang and McFarlane 1995) and
138 shallow convective (Park and Bretherton 2009) schemes, moist boundary layer turbulence scheme
139 (Bretherton and Park 2009), and Rapid Radiative Transfer Model for GCMs (RRTMG; Mlawer
140 et al. 1997) scheme. Therefore, CAM-SE and CAM-FV differ primarily in their dynamical cores,
141 which has previously been shown to impact the simulation of TC climatology in the model (Reed
142 et al. 2015). The prescribed SST and sea-ice boundary dataset for both simulations is provided
143 from Hurrell et al. (2008).

144 The sixth atmosphere-only model simulation we analyze is one member of the M2-AMIP (for
145 Modern-Era Retrospective Analysis for Research and and Applications, Version 2 (MERRA-2;
146 Gelaro et al. 2017) Atmospheric Model Intercomparison Project (AMIP)) set of simulations (Col-
147 low et al. 2017, 2018) performed with the NASA Goddard Earth Observing System Model Ver-
148 sion 5, version 5.12.4 (GEOS; Rienecker et al. 2008; Molod et al. 2015). This version of the
149 atmosphere component of GEOS is the same model that was used for MERRA-2, the most re-
150 cent NASA re-analysis data product, but the simulation we analyze is a free-running version of
151 the model initialized in November 1979 and driven by the MERRA-2 SST and sea-ice boundary
152 conditions (Bosilovich et al. 2015). GEOS employs a finite volume dynamical core (Putman and
153 Lin 2007) with a c180 cubed-sphere grid (an approximate horizontal resolution of 50 km), which
154 is then spatially interpolated to a $0.625^\circ \times 0.5^\circ$ longitude-latitude grid. The native model vertical
155 grid has 72 terrain-following hybrid-eta levels. GEOS employs a Relaxed Arakawa-Schubert con-
156 vection scheme (Moorthi and Suarez 1992) and parameterizations for longwave (Chou and Suarez
157 1994) and shortwave (Chou and Suarez 1999) radiation; other details on the physics packages can
158 be found in Molod et al. (2015).

159 *b. TC detection and tracking*

160 TC-like vortices (which we refer to as ‘TCs’) are detected and tracked from the model fields
161 using standard tracking algorithms from each modeling group, which produce, for each TC, a time
162 series of the TC’s center longitude and latitude, minimum sea level pressure, and maximum wind
163 speed corrected to a surface (10 m) value (V_{max}). We use V_{max} to characterize the TC intensity.

164 The TCs in the HiRAM simulation are tracked using the routine described in Zhao et al. (2009),
165 which is based on Vitart et al. (1997, 2003) and Knutson et al. (2007). This algorithm locates grid
166 points with an 850 hPa relative vorticity maximum, local sea level pressure minimum, and warm

167 core, and tracks the storm by searching for a vortex in the next snapshot within a distance of 400
168 km and connecting the snapshots. It requires that storms last at least 3 days and have a maximum
169 surface wind speed greater than 17 ms^{-1} during at least 3 (not necessarily consecutive) days.

170 The tracking scheme used in AM2.5 and FLOR is similar to that used in HiRAM and is described
171 in Murakami et al. (2015) and Harris et al. (2016). This algorithm uses local sea level pressure
172 minimum and a warm core criteria to detect TCs and requires that storms last at least 3 days, be
173 warm-core for at least 2 days, and have a maximum surface wind speed greater than 15.75 ms^{-1}
174 during at least 36 hours while the storm has a warm core.

175 The TCs in the CAM-SE simulation are tracked using TempestExtremes (Ullrich and Zarzycki
176 2017; Zarzycki et al. 2017), while the TCs in the CAM-FV simulation are tracked using the de-
177 tection algorithm from Zhao et al. (2009). TempestExtremes (Ullrich and Zarzycki 2017; Zarzycki
178 et al. 2017) searches for a local minimum in sea level pressure and a collocated local maximum in
179 geopotential thickness between the 300 and 500 hPa levels (which indicates a warm core). Can-
180 didate cyclones are then stitched together in time, with storms needing to be equatorward of 40°
181 latitude for at least 60 hours (not necessarily consecutive) and separate trajectories which termi-
182 nate and begin within 12 hours and 10° s of one another are merged to eliminate double-counting
183 of broken tracks.

184 The TCs in the GEOS simulation are tracked using the Camargo and Zebiak (2002) tracking
185 algorithm, which has been widely applied to various global and regional climate models (e.g.,
186 Camargo 2013). This algorithm uses basin-dependent thresholds of low level vorticity, surface
187 wind speed, and vertically integrated temperature anomaly to detect TCs, then tracks the low level
188 vorticity center forward and backward in time from each point that has met the detection criteria.
189 For this study, we additionally require that the vortex have a maximum surface wind greater than
190 15.2 ms^{-1} for 3 days (not necessarily consecutive). If this threshold is not applied, the Camargo and

191 Zebiak (2002) algorithm detects many more weak storms, which shifts the intensity distribution
192 in GEOS towards weaker wind speeds and increases the sample size of total storms, but does not
193 otherwise have a significant impact on our results or conclusions.

194 **3. Analysis Methodology**

195 For all models except CAM-SE, we use two years of 6-hourly output to apply our analysis along
196 individual simulated tropical cyclone tracks. Eight years, 1992-1999, are analyzed for the CAM-
197 SE simulation, so that the number of TCs analyzed is comparable to the other models, since we
198 only analyze TCs in the North Atlantic in CAM-SE, compared with the global distribution of TCs
199 in the other models. GCM outputs are saved with a 6-hour time interval on model levels (several
200 of the models provided output at 3-hour or 1-hour time intervals, but since we track the tropical
201 cyclones in 6-hour increments, we do not make full use of the higher temporal sampling). We
202 perform our analysis in 10° boxes centered on each TC and following each TC. When making
203 composites, we exclude points over land and TCs that have moved poleward of 30° . The number
204 of TCs analyzed in each model is shown in Table 2.

205 We compute budgets of column-integrated moist static energy and spatial variance of column-
206 integrated moist static energy. Moist static energy is approximately conserved under moist adia-
207 batic processes and its column integral is unchanged by convection. The analysis framework for
208 the variance budget was first developed by Wing and Emanuel (2014) to understand the physical
209 mechanisms of self-aggregation of convection in idealized simulations. It has since been applied
210 to simulations of tropical convection in a variety of idealized and realistic configurations (Arnold
211 and Randall 2015; Wing and Cronin 2016; Coppin and Bony 2015; Holloway and Woolnough
212 2016; Becker et al. 2017; Holloway 2017) and to cloud-resolving model simulations of tropical

213 cyclones (Wing et al. 2016). Column-integrated moist static energy, \widehat{h} , is given by

$$\widehat{h} = \frac{1}{g} \int_{p_t}^{p_b} (c_p T + gz + L_v q) dp, \quad (1)$$

214 where p_t is the pressure at the model top, p_b is the pressure at the bottom, q is water vapor mixing
 215 ratio, and all other variables have their usual meaning. Usually, one would perform the integral
 216 using the surface pressure as p_b . Here, we perform our analysis on model levels using the 4-
 217 D varying pressure (calculated using the surface pressure and the appropriate relation for each
 218 model’s hybrid vertical coordinates). This causes difficulties with the evaluation of the column
 219 integral, since one of its bounds (the surface pressure) decreases dramatically over the life cycle
 220 of a tropical cyclone. To avoid complications in the interpretation of the variability of moist static
 221 energy in and around the TC due to decreasing column mass, we interpolate the moist static energy
 222 to a fixed pressure level of $p_b = 920$ hPa, and integrate from there to the next model level above,
 223 and then through the rest of the column on model levels. This may introduce some error to the
 224 closure of the moist static energy budget, as the other terms (described below) are evaluated at the
 225 surface rather than at 920 hPa. The budget for column-integrated moist static energy is given by

$$\frac{\partial \widehat{h}}{\partial t} = F_k + N_L + N_S - \widehat{\vec{u} \cdot \nabla h}, \quad (2)$$

226 where F_k is the surface enthalpy flux, N_L is the column longwave radiative flux convergence, and
 227 N_S is the column shortwave radiative flux convergence. Each of these terms (as well as advection,
 228 the last term on the right hand side of Equation (2)) is a source or sink of \widehat{h} . F_k , N_L , and N_S
 229 are output as temporal averages (6-hourly for HiRAM, AM2.5, and FLOR, 3-hourly for CAM-
 230 SE and CAM-FV, and 1-hourly for GEOS); we average consecutive periods together to derive
 231 a value centered around the time of the TC snapshot. \widehat{h} is computed as described above, using
 232 instantaneous output at the time of the TC snapshot, and $\frac{\partial \widehat{h}}{\partial t}$ is computed using a centered finite
 233 difference. Given the uncertainties associated with calculating the advection of moist static energy

234 from offline model output, we calculate the advective term as a residual from the rest of the budget.
 235 All terms are computed at each grid point within the 10° box centered on the TC.

236 The budget for the spatial variance of \widehat{h} is given by

$$\frac{1}{2} \frac{\partial \widehat{h}'^2}{\partial t} = \widehat{h}' \frac{\partial \widehat{h}'}{\partial t} = \widehat{h}' F'_k + \widehat{h}' N'_L + \widehat{h}' N'_S - \widehat{h}' (\widehat{\mathbf{u}} \cdot \nabla \widehat{h})', \quad (3)$$

237 where primes indicate anomalies from the mean of the $10^\circ \times 10^\circ$ box centered around a TC. As
 238 convection organizes and the TC forms, the convecting areas become moister and the surrounding
 239 non-convecting areas become drier. This is manifest as an increase in the spatial variance of \widehat{h}
 240 computed over a box surrounding the developing storm. Each of the terms on the right hand side
 241 of Equation (3) measures the contribution of a feedback to the increase in \widehat{h} variance; a positive
 242 feedback indicates that the processes amplifies \widehat{h} anomalies, such as enhanced surface fluxes in an
 243 area of already moister than average air. In idealized simulations, the moist static energy variance
 244 always increases as the TC forms and intensifies (Wing et al. 2016), but this does not necessarily
 245 have to generalize to more realistic simulations (or nature). We examine whether the moist static
 246 energy variance increases with TC intensification in the climate model simulations, but note that
 247 even if this relationship does not always strictly hold, it is still informative to examine how the
 248 different terms in the budget contribute to the variance tendency.

249 We calculate each term in the two budgets at each grid point in the box following the tracks of
 250 each simulated TC. We then composite over the simulated TCs in two different ways:

- 251 1. A life cycle composite, where all snapshots at the same time relative to the time of lifetime
 252 maximum intensity (LMI) of each TC are averaged together; and
- 253 2. An intensity-bin composite, where all snapshots in which the TC has a maximum near surface
 254 wind speed in a given range are averaged together.

255 In the life cycle composite, we examine times prior to the LMI in 6-hour increments, and go
256 backwards in time until the composite contains less than 25% of the total TCs (the lifetime varies
257 from storm to storm). This allows us to assess how different processes are contributing to the
258 formation and intensification of the composite TC in each model as it moves through its life cycle,
259 and can be compared to similar analysis for idealized TCs simulated with explicit convection
260 (Wing et al. 2016). When comparing the different models, however, the average intensity may
261 be quite different at the same life cycle stage, which may contribute to a feedback being stronger
262 or weaker. This motivates the use of the intensity-bin composite, following Kim et al. (2018),
263 in which the model-to-model comparison is made using TC snapshots at the same intensity (the
264 maximum near surface wind at each TC snapshot, as determined by the tracking algorithm). Only
265 TC snapshots up until the time of the LMI of a given storm are included in the composite. The
266 intensity bins used for this composite analysis and the number of snapshots in each bin are given
267 in Table 3.

268 **4. Results**

269 *a. General characteristics of TC simulation*

270 As an overview of the TC climatology in the six simulations we examine, the genesis positions
271 for the tracked TCs in each model, and in the best-track observational data ¹, is shown in Figure
272 1. While all models have reasonable spatial distributions and genesis frequency of TCs, there
273 are large differences between them and clear biases compared to the observations. Many of the
274 models struggle to accurately simulate the genesis distribution in the North Atlantic, for example.
275 Overall, HiRAM and FLOR seem to form the most TCs, which is also true in the two years of data

¹Tracks in the North Atlantic and eastern North Pacific are from the National Hurricane Center (Landsea and Franklin 2013) and tracks in other basins are from the Joint Typhoon Warning Center (Chu et al. 2002)

276 we analyze in detail (Table 2). Note that it is expected that CAM-SE generates few TCs outside of
277 the Atlantic because the high resolution region is confined to only that basin.

278 The intensity distribution for the simulated TCs in each model is shown in Figure 2 (only for
279 the two years that are analyzed - see Table 2 - and, for CAM-SE, only for TCs in the North
280 Atlantic). CAM-SE has a greater likelihood of simulating storms at the high intensity tail of the
281 distribution than CAM-FV, consistent with Reed et al. (2015), though the mean LMI is higher in
282 CAM-FV. Overall, CAM-SE and CAM-FV simulate significantly stronger storms than the other
283 four models, as expected due to their finer grid spacing. However, resolution is not the only source
284 of inter-model spread in intensity. The TCs in HiRAM are noticeably stronger than those in AM2.5
285 and FLOR, despite those models having the same resolution and dynamical core. All the models
286 have a low intensity bias compared to the best-track observations (dashed line in Figure 2a). Only
287 a few of the models show evidence of the observed bimodal distribution of intensity, where the
288 secondary peak in LMI is associated with storms that undergo rapid intensification (Lee et al.
289 2016).

290 The multiple tracking algorithms used across the simulations could contribute to these differ-
291 ences. cursory analysis found minimal differences in TC statistics in the CAM-SE and CAM-FV
292 simulations, limited to weaker storms, when applying both the Zhao et al. (2009) and Tempest-
293 Extremes algorithms to the same dataset (not shown). We performed more in-depth analysis (re-
294 peating all calculations described in subsequent sections) for the case in which the GFDL tracking
295 algorithm (used for AM2.5 and FLOR; Murakami et al. 2015; Harris et al. 2016) was also applied
296 to HiRAM (cyan-curve in Figure 2, referred to as HiRAM-G). When applied to the HiRAM simu-
297 lation, the GFDL algorithm yields weaker TCs than the HiRAM (Zhao et al. 2009) algorithm does
298 (blue curve in Figure 2). We speculate that this is because the Murakami et al. (2015) implemen-
299 tation of the Harris et al. (2016) algorithm has less strict wind speed conditions for detecting TCs

300 than does the HiRAM algorithm, allowing the GFDL algorithm to detect more weaker TCs, and
301 to track those TCs for longer, which impacts the likelihood of observing any individual intensity
302 (note that for an individual TC snapshot at the same time and location, the two algorithms yield
303 the same intensity). Importantly, we find that the sensitivity to tracking algorithm does not cause
304 any significant differences in the results of our moist static energy variance budget analysis. Some
305 of the terms in the moist static energy variance budget have slightly smaller values in HiRAM-G
306 than in HiRAM (not shown), but this does not change the comparison to the other models or any
307 of our conclusions.

308 *b. Moist static energy budget*

309 We first examine the evolution of the moist static energy budget over the composite TC life cycle
310 (Equation 2). Each term in the moist static energy budget composited 48 hours prior to the LMI
311 of the simulated TCs is shown, for the CAM-FV simulation, in Figure 3. The signature of the TC
312 can be easily seen in the spatial distribution of column moist static energy, which is larger near the
313 TC center due to the warm, moist air there (Figure 3b). The moist static energy of the composite
314 TC generally increases as it intensifies towards its LMI, as can be seen in an animation of the
315 evolution of the moist static energy budget with time over the composite TC life cycle (found in
316 the supplementary material), and in the positive tendency of \hat{h} in the vicinity of the TC (Figure
317 3c). The column radiative flux convergence is generally negative (cooling) and thus a sink of
318 moist static energy. At this particular time, however, it is actually slightly positive (indicating net
319 column radiative heating) in the vicinity of the TC (Figure 3d), which reflects the influence of the
320 moist air and thick cloud shield associated with the TC. The surface enthalpy fluxes are positive,
321 and are therefore a source of moist static energy (Figure 3e). They are larger in the vicinity of the
322 TC because of the larger surface winds there. The advection of moist static energy is generally

323 negative and downgradient, though since this term is calculated as a residual, we cannot be certain
324 that it is entirely and only representing advection (Figure 3f). These relationships are also found
325 in the other models; equivalent figures and animations for the other five models are provided in
326 the supplementary material.

327 *c. Moist static energy variance budget*

328 As noted above, the moist static energy of the TC increases as the TC forms and intensifies, and
329 in particular, it increases relative to the moist static energy of the surrounding environment. This
330 should be reflected in an increase in the spatial variance of the moist static energy. To quantify
331 the feedbacks that may contribute to a change in the spatial variability of \hat{h} , we now examine the
332 \hat{h} variance budget over the composite TC life cycle (Equation 3). Each term in the \hat{h} variance
333 budget composited 48 hours prior to the LMI of the simulated TCs is shown, for the CAM-FV
334 simulation, in Figure 4. As could be inferred from Figure 3, \hat{h} is anomalously high in the vicinity
335 of the TC. The tendency of \hat{h}^2 is noisy but positive near the TC center (Figure 4c). Both the
336 radiative and surface flux feedbacks are positive, indicating that both of these processes contribute
337 to the amplification of \hat{h} anomalies. The radiative feedback is positive throughout the domain,
338 but largest near the center of the TC where the anomalously high \hat{h} is coincident with reduced
339 column radiative cooling associated with thick cloud cover (Figure 4d). The surface flux feedback
340 is most positive near the TC eyewall, where the largest surface winds (which enhance the surface
341 fluxes) are found and where \hat{h} is large; it is near zero at the center of the TC because the winds are
342 calmer there (Figure 4e). There are some areas in the environment away from the TC where the
343 surface flux feedback is slightly negative (tending to damp \hat{h} anomalies). This is because surface
344 enthalpy fluxes depend both on surface wind speed and air-sea enthalpy disequilibrium, and the
345 two influences generally oppose each other (Wing et al. 2016). The advective term is negative,

346 indicating that advection of \hat{h} damps \hat{h} anomalies (Figure 4f). Equivalent figures and animations
347 for the other five models are provided in the supplementary material.

348 Across all models, though to a lesser extent in FLOR and GEOS, the surface flux feedback
349 is positive near the TC and becomes larger as the TC approaches the LMI (Figures 5, 6, 7, and
350 8). The radiative feedback is also positive across all models but, with the exception of GEOS, is
351 smaller than the surface flux feedback. It also generally increases with intensification towards the
352 LMI, though the relative rate of increase is slower than that of the surface flux feedback (Figures 5,
353 6, 7, and 8). The feedback terms generally increase with intensification because the anomalously
354 high values of moist static energy, surface fluxes and cloud-induced reduction in radiative cooling
355 increase as the TC develops and matures. While the structure of these feedback terms is similar
356 across all models, there are notable differences in their strengths (e.g., Figure 7). The models that
357 produce stronger storms, both overall and at the time of the composite, have stronger feedbacks
358 (CAM-SE, CAM-FV, and HiRAM), especially with regard to the surface flux feedback. In the
359 two models with the highest resolutions, CAM-SE and CAM-FV, and in GEOS, the surface flux
360 feedback is near zero at the center of the TC, indicating a reduction of the winds near an eye-like
361 feature. This is not as apparent in the other models.

362 One possible explanation for the differences in the magnitudes of feedbacks across the models
363 is that they may simply have different absolute values of moist static energy and its variability. To
364 adjust for this, we normalize the feedback terms by the value of the box average \hat{h} variance at a
365 given time, then perform the composite. An example of this analysis, for the composite 48 hours
366 prior to LMI, is shown in Figure 9 (other times are shown in the supplementary material). The
367 differences between models remain, particularly in the surface flux feedback. There are minimal
368 model-model differences in the radiative feedback, which indicates that the radiative feedback is

369 *relatively* more important in the models with weaker surface flux feedbacks and weaker storms
370 (AM2.5, FLOR, and GEOS).

371 *d. Box-average variance budget*

372 The above analysis shows the contribution of different terms to the \hat{h} variance on a grid point-
373 by-grid point basis, but it is also informative to examine the box-average budget. This is computed
374 by, for each TC and track point, averaging the squared \hat{h} anomalies and each term in the variance
375 budget over the box surrounding the TC, and then taking a composite over the same time relative to
376 LMI. The composite box-average \hat{h} variance generally increases as the LMI is approached (Figure
377 10a-f), though individual TCs do not always have a monotonic increase in \hat{h} variance over their life
378 cycle (in part because individual TCs do not always have a monotonic increase in intensity). We
379 find that an increase in the box-average \hat{h} variance with TC formation and intensification is more
380 robust in the stronger TCs. Therefore, for the calculation of the life cycle composite box-average
381 \hat{h} variance budget, we restrict our analysis to the storms whose LMI is in the upper quartile of the
382 LMI distribution (Figure 10).

383 The evolution of the terms in the box-average \hat{h} variance budget throughout the TC life cycle
384 is qualitatively similar across the models and similar to the behavior of an idealized TC in cloud-
385 resolving simulations (Wing et al. 2016). The surface flux and longwave radiative feedback are the
386 two main contributors to increases in box-average \hat{h} variance. Early in the TC life cycle, the two
387 have similar magnitudes, but as the TC intensifies towards its LMI, the surface flux feedback in-
388 creases substantially (as a result of the increasing surface wind speed, which drives higher surface
389 fluxes near the TC). This is apparent in the HiRAM, CAM-SE, and CAM-FV simulations (which
390 have the strongest TCs) and consistent with the results of Wing et al. (2016). In the other models,
391 the surface flux feedback increases only slightly, if at all. In FLOR and GEOS (which have the

392 weakest TCs), the box-average surface flux feedback is actually smaller than the longwave radia-
393 tive feedback throughout the composite TC life cycle. These results indicate that, not only do the
394 values of the feedback terms differ from model to model, but so does the relative importance of
395 a given feedback compared to the other feedbacks. Across all models, the shortwave feedback is
396 very small (so the radiative feedback is dominated by spatial variability in the longwave cooling)
397 and the advection (residual) term is negative.

398 Whether measured by the maximum intensity produced by any storm in the simulation or the
399 average LMI of all the TCs, the models that simulate more intense storms have larger box-average
400 surface flux feedbacks (Figure 11; shown for the composite 48 hours prior to LMI, but the results
401 are similar at other times). The box-average radiative feedback, on the other hand, does not vary
402 much across models. It follows that the models with stronger storms have a higher ratio of com-
403 posite mean box-average surface flux feedback to radiative feedback (Figure 11b). That is, while
404 both surface flux and radiative feedbacks contribute to increased \hat{h} variance and TC development
405 in all models, the surface flux feedback contributes *relatively* more in the models with stronger
406 storms. This points to the importance of spatially varying surface fluxes (primarily driven by wind
407 speed variability) for the simulation of TCs.

408 We note in passing that one potential limitation of this analysis is that the same sized-box was
409 used for all six models and for all TCs in each model. Unlike idealized simulations where there is
410 one TC in a homogenous domain (Wing et al. 2016), in these realistic simulations, a box size must
411 be chosen such that it is large enough to contain the TC as well as the environment surrounding it,
412 but not so large that it contains other disturbances. A larger or smaller box may therefore be more
413 appropriate for larger or smaller TCs (and the minimum TC size is limited by the grid resolution,
414 which varies between models), but for the purposes of the present study we emphasize simplicity
415 and consistency by using a fixed $10^\circ \times 10^\circ$ box size.

416 *e. Composite over intensity bins*

417 While the life cycle composite discussed in Sections 4b-d is useful for examining how different
418 feedbacks contribute to the increase in \hat{h} variance throughout the TC life cycle in each model,
419 the difference in feedback magnitudes across the models could also be an artifact of the fact that,
420 though the composite is taken at the same stage in the TC life cycle, the intensities at that time are
421 different (see, for example, the first row of Figure 7). The surface flux feedback explicitly depends
422 on the TC intensity because of the dependence of surface fluxes on surface wind speed. Therefore,
423 we also analyze an intensity-bin composite, as described in Section 3.

424 Despite being compared at the same TC intensities, there are differences in the moist static
425 energy and its sources and sinks across the models (see Figure 12 for the 24-27 ms^{-1} bin; other
426 bins are in the supplementary material). GEOS stands out by having noticeably smaller values
427 of moist static energy overall and stronger radiative cooling (more negative) in the environment
428 around the TC (Figures 12f and l). The other models look fairly similar to each other, with the
429 biggest difference being in the strength of the surface fluxes near the center of the TC. CAM-
430 SE has the strongest surface fluxes, followed by CAM-FV, HiRAM, AM2.5, GEOS, then FLOR
431 (Figure 12). There are also slight differences in the radiative cooling; the reduced radiative cooling
432 associated with thick cloud cover over the TC is spread over a larger area in HiRAM, AM2.5, and
433 FLOR. This could be related to the coarser resolution of these models compared to CAM-SE and
434 CAM-FV.

435 The different spatial structures of moist static energy, radiative cooling, and surface fluxes in
436 Figure 12 are reflected in model-model differences in the feedback terms in the \hat{h} variance budget,
437 shown for three different intensity bins in Figures 13, 14, and 15. The structure of \hat{h}^2 and the
438 feedback terms is similar across the intensity bins, but the magnitude generally increases with

439 intensity. One anomaly is the surface flux feedback in the CAM-SE simulation in the 15-18 ms^{-1}
440 bin (Figure 13m), which is likely due to the relative few samples included in that bin, some of
441 which may have areas of land that are masked out. The main conclusion from Figures 13, 14,
442 and 15 is that even when composited over the same intensities, there are notable differences in the
443 strength of the surface flux feedback between models. The surface flux feedback near the center of
444 the TC is strongest in CAM-SE and CAM-FV, which are the models that simulated the strongest
445 TCs, followed by HiRAM, AM2.5, GEOS, and FLOR (Figures 14 and 15). The interpretation
446 of this result is that, at a given intensity, certain models have a stronger surface flux feedback
447 than others, which favors further amplification of \hat{h} anomalies and further intensification of the
448 TC, to the extent that \hat{h} and surface winds are related. With the exception of GEOS, which has
449 a notably strong radiative feedback, the radiative feedbacks are similar across the models. As in
450 Section 4c, we also examine the intensity-bin composite where each term has been normalized by
451 the box-mean \hat{h} variance. The general result that the surface flux feedback differs across models
452 is robust (see for example the 24-27 ms^{-1} composite in Figure 16; other bins are shown in the
453 supplementary material.)

454 The value of the intensity-bin composite is made clear in Figure 17, which shows the box-
455 average \hat{h} variance and surface flux and radiative feedbacks composited over each 3 ms^{-1} intensity
456 bin. There is a clear tendency for the \hat{h} variance to be higher at higher wind speeds, though the
457 absolute value of \hat{h} variance differs across models, especially on GEOS (Figure 17a). There is a
458 strong dependence of the surface flux feedback on the wind speeds over which it is composited,
459 with the higher intensity bins having surface flux feedbacks that are 2-3 times stronger than lower
460 intensity bins (Figure 17b). The radiative feedback, on the other hand, is only weakly dependent
461 on the wind speed over which it is composited (Figure 17c). The surface flux feedback in CAM-
462 SE and CAM-FV is similar across most intensity bins, while the radiative feedback in CAM-

463 FV becomes larger above the 30 ms^{-1} bin. This reflects the fact that the overall TC intensity
464 distributions in CAM-SE and CAM-FV are similar; while CAM-FV has an LMI distribution that
465 is shifted towards stronger storms (Figure 2a), CAM-SE has an overall higher probability of TC
466 snapshots at higher intensities (Figure 2b). Between $20\text{-}35 \text{ ms}^{-1}$, AM2.5 has a notably stronger
467 surface flux feedback than FLOR (Figure 17a) - recall that AM2.5 simulates more intense TCs
468 than FLOR does (Figure 2). Above the 25 ms^{-1} bin, HiRAM has a significantly stronger surface
469 flux feedback than AM2.5; suggesting that this allows the TCs in HiRAM to eventually become
470 stronger than those in AM2.5. GEOS is a bit of an outlier; while the weak surface flux feedback
471 is consistent with the fact that GEOS simulates weaker TCs, the radiative feedback and \hat{h} variance
472 itself are much stronger than in the other models.

473 These results are summarized in Figure 17d, which shows both the box-average surface flux and
474 radiative feedbacks composited over the $24\text{-}27 \text{ ms}^{-1}$ bin in each of the models. There is a clear
475 tendency for the box-average surface flux feedback to be larger in the models that simulate TCs
476 with higher mean LMI, while the radiative feedback does not vary much between models.

477 5. Discussion

478 There are several informative comparisons that can be made by comparing individual pairs of
479 models in the set of six examined here. CAM-SE and CAM-FV differ primarily in their dynamical
480 core, which has been shown to affect simulated TC intensity and frequency, with the spectral
481 element core producing stronger TCs (Reed et al. 2015). In the simulations we examined, the
482 distribution of LMI in CAM-SE was wider than that in CAM-FV, with a higher relative frequency
483 of both weak and strong storms (Figure 2a). However, the comparison between CAM-SE and
484 CAM-FV presented here is not an apples-to-apples comparison because the CAM-SE distribution
485 includes only storms in the North Atlantic (which may have weaker storms than other basins, such

486 as the western North Pacific), includes different years than the CAM-FV simulation, and uses a
487 different tracking algorithm. When TCs in the North Atlantic in 1996-1997 are analyzed for both
488 CAM-SE and CAM-FV, the TCs in CAM-SE are found to reach higher intensity more frequently
489 (Moon et al. 2018), consistent with Reed et al. (2015). We showed that CAM-SE tends to have
490 a stronger surface flux feedback than CAM-FV near the center of the TC within 48 hours of the
491 time of LMI and that, when storms in the upper quartile of the LMI distribution are considered,
492 the box-average surface flux feedback is also larger in CAM-SE. The surface flux feedback was
493 also found to be slightly stronger in CAM-SE than CAM-FV when considering a composite at the
494 same intensity.

495 HiRAM and AM2.5 differ only in their choice of convection scheme, and HiRAM simulates
496 notably stronger TCs than AM2.5 (Figure 2). Kim et al. (2018) linked this to both larger surface
497 fluxes and greater rainfall amounts (and therefore diabatic heating) in the inner-core regions of
498 TCs in HiRAM compared to AM2.5. This is consistent with our analysis, in which the surface
499 flux feedback was notably stronger in HiRAM than in AM2.5, both at the same stage in the TC
500 life cycle and at the same intensity. The radiative feedback was found to be slightly stronger in
501 HiRAM, though the difference was small compared to the difference in surface fluxes.

502 AM2.5 and FLOR differ only in that FLOR is a coupled ocean-atmosphere model, while AM2.5
503 is an atmosphere-only model. AM2.5 simulates stronger TCs than FLOR (Figure 2), and this
504 too appears to be linked to a stronger surface flux feedback in in AM2.5. Ocean coupling is
505 known to reduce TC intensity, because the cold wake generated by TC-driven upwelling is a
506 negative feedback on the TC (e.g., Lloyd and Vecchi 2011; Zarzycki 2016; Zarzycki et al. 2016;
507 Scoccimarro et al. 2017). Here, we show explicitly that ocean coupling also reduces the surface
508 flux feedback, as defined in the \hat{h} variance framework. This is significant because, in the context of
509 convective self-aggregation, these surface flux feedbacks have only been examined in simulations

510 with fixed SST (e.g., Wing and Emanuel 2014; Coppin and Bony 2015; Wing and Cronin 2016).
511 The reduction in the surface flux feedback with ocean coupling is consistent with studies that have
512 found that ocean coupling delays self-aggregation (Hohenegger and Stevens 2016).

513 Why would the surface flux feedback differ across models? In general, the sign and magnitude
514 of the surface flux feedback depends on the spatial co-variability of column-integrated moist static
515 energy and surface fluxes. The spatial variability of surface fluxes in turn depends on the spatial
516 variability in surface wind speed and air-sea enthalpy disequilibrium. Therefore, this feedback
517 could be larger in a given model because of (i) higher moist static energy near the TC and/or lower
518 moist static energy in the surrounding environment, (ii) larger values of surface fluxes near the
519 center of the TC because of stronger winds or larger air-sea disequilibrium (though the latter is
520 unlikely to be large near the center of the TC), or (iii) better alignment between the location of
521 the high values of surface fluxes (usually near the strongest winds) and the location of highest
522 moist static energy. Even when evaluated at the same intensity, the overall structure of the TC
523 wind field may be different across different models. Differences in the representation of boundary
524 layer processes or frequency of coupling to the surface could lead to different surface fluxes, and
525 differences in the representation of moist convection could lead to different patterns of humidity.

526 With regards to CAM-SE and CAM-FV, Figure 12 indicates that the surface fluxes themselves
527 are larger near the TC center in CAM-SE. Moon et al. (2018) found that this is mostly due to a
528 difference in the latent heat flux, and that this was mostly due to a larger air-sea enthalpy dise-
529 quilibrium in CAM-SE. It is not clear what about the different dynamical cores could cause this
530 difference, but one possibility is a difference in how the physics-dynamics coupling is configured.
531 More generally, differences in divergence damping have also been proposed as a reason for the
532 sensitivity of TC simulation to dynamical core (Zhao et al. 2012).

533 GEOS, which has similar horizontal resolution as HiRAM, AM2.5, and FLOR, simulates the
534 weakest storms and the weakest surface flux feedback compared to other models when compared
535 at the same intensity. But, GEOS has a larger (more positive) radiative feedback than the other
536 models, both when compared at the same intensity and at the same stage in the TC life cycle -
537 which is a difference in the *opposite* direction of one that would explain the weaker storms. We
538 speculate that the difference in radiative feedback originates from details in the convection and
539 cloud schemes (such as cloud lifetimes and detrainment) or possible mean state differences, but
540 an in-depth investigation is beyond the scope of this study. We also note that, when the 15.2 ms^{-1}
541 threshold is applied, GEOS has much fewer storms than the other models (and observations). This
542 is consistent with Lim et al. (2015), who found that realistic numbers of TCs were difficult to
543 achieve with 0.5° grid spacing without modifying the values for TC detection.

544 The life cycle composites (Sections 4c-d) also indicate that, in TCs simulated by high-resolution
545 GCMs, the radiative feedback is at least as important as the surface flux feedback in the early
546 stages of TC development, and in some models, it remains as important throughout intensification
547 to LMI. This result adds to a growing body of evidence on the importance of radiation in TC
548 formation, intensification, and structure (Fovell et al. 2010; Bu et al. 2014; Melhauser and Zhang
549 2014; Nicholls 2015; Navarro and Hakim 2016; Tang and Zhang 2016; Fovell et al. 2016; Wing
550 et al. 2016; O'Neill et al. 2017; Bu et al. 2017). It is consistent with the cloud-resolving model
551 results of Wing et al. (2016), which found a similar role for the radiative feedback in the evolution
552 of a spontaneously generated TC in radiative-convective equilibrium simulations, and that removal
553 of radiative feedbacks inhibits or significantly delays the onset of genesis. The positive radiative
554 feedbacks diagnosed in this study result from the direct effect of differential heating between the
555 area of deep convection in the developing TC and the surrounding, drier environment, which acts to
556 favor ascent and moistening in the already moist area. This promotes clustering of convection and

557 continued moistening of the atmosphere, both of which further the formation of a tropical cyclone.
558 The differential heating can also indirectly favor TC formation by the generation of a circulation
559 response (Nicholls 2015; Muller and Roms 2018), though this is not explicitly quantified by our
560 \widehat{h} variance budget diagnostic. Our results indicate that it is specifically the variability in longwave
561 radiation due to clouds (Figure 10) that drives the positive radiative feedback.

562 **6. Conclusions**

563 We have developed and applied process-oriented diagnostics utilizing budgets of column moist
564 static energy and the spatial variance of column moist static energy to tropical cyclones in six
565 high-resolution climate models. These diagnostics allow us to quantify different feedbacks related
566 to how convection, moisture, clouds, and related processes are coupled.

567 We found that the general evolution of the moist static energy variance budget along the com-
568 posite TC life cycle is qualitatively similar to that found in idealized cloud-resolving model sim-
569 ulations. The box-average moist static energy variance is higher at higher wind speeds, both in
570 the life cycle and intensity-bin composites. Surface flux and radiative feedbacks both contribute
571 positively, and fairly equally, to an increase in moist static energy variance in the early stages of
572 TC formation and intensification. As the TC nears its lifetime maximum intensity, the surface
573 flux feedback increases beyond the magnitude of the radiative feedback (which is dominated by
574 longwave-cloud effects) in most, though not all models. At the same point in the TC life cycle,
575 the models that simulate stronger storms have stronger surface flux feedbacks, while the radia-
576 tive feedback is more consistent across models. This indicates that the radiative feedbacks are
577 relatively more important to TC formation and intensification in models with weak storms. The
578 difference in surface flux feedback across the models is robust even when we consider composites
579 over the same intensity.

580 In particular, CAM-SE and CAM-FV simulate the strongest storms and have the strongest sur-
581 face flux feedbacks, and are even slightly different from each other despite the only difference be-
582 ing the dynamical core. HiRAM has notably stronger storms and stronger surface flux feedbacks
583 than do AM2.5 or FLOR, despite all three models being at the same resolution and using same
584 dynamical core - indicating the importance of physics parameterizations, especially the convection
585 scheme, as has also been noted by other studies. AM2.5 has stronger storms and a stronger sur-
586 face flux feedback than FLOR, indicating that ocean coupling reduces the strength of the surface
587 flux feedback. GEOS has the weakest storms and weakest surface flux feedback, but, curiously, a
588 stronger than average radiative feedback.

589 The inter-model spread in surface flux feedbacks results from a difference in the spatial co-
590 variability in moist static energy, surface wind speed, air-sea disequilibrium, and surface enthalpy
591 fluxes between the different models, which is linked to the model representation of the spatial
592 structure of the TC wind and moisture field. Overall these results indicate that the representation
593 of the interaction of spatially varying surface fluxes with the developing TC is partially responsible
594 for inter-model spread in TC simulation, in which stronger variability of surface fluxes between
595 the TC core and its surroundings leads to stronger TCs. Our results also indicate that the radiative
596 feedback contributes to TC development across all models, especially at weaker intensities or in
597 earlier stages of development.

598 These results show that the moist static energy variance budget is a useful tool for examining
599 tropical cyclone formation and intensification in models, with links to the actual physical processes
600 responsible for model simulation of TCs. However, while it is able to distinguish between models,
601 there does not yet exist an observational “reference” version of this diagnostic, so it is unknown
602 which models’ representation of surface flux and radiative feedbacks is “correct”. Creating a

603 reference diagnostic from observations of TCs, as well as applying this diagnostic to a broader
604 range of models, will be the subject of future work.

605 *Acknowledgments.* This work is a contribution to the process-oriented diagnostic effort of the
606 NOAA MAPP Model Diagnostics Task Force. This study was supported by NOAA's Cli-
607 mate Program Office's Modeling, Analysis, Predictions, and Projections program through Grant
608 NA15OAR4310087. Initial work on this study was performed while A. Wing was supported by a
609 NSF AGS Postdoctoral Research Fellowship (AGS-1433251). Y. Moon was supported in part by
610 a NSF AGS Postdoctoral Research Fellowship (AGS-1524270). We thank Salvatore Pascale and
611 Lucas Harris for constructive comments on the manuscript. We thank Michael Bosilovich for fa-
612 cilitating access to the GEOS M2-AMIP data and providing additional information about the sim-
613 ulation. The M2-AMIP data is now publicly available through the NASA Center for Climate Sim-
614 ulation (NCCS) DataPortal (https://portal.nccs.nasa.gov/datashare/gmao_m2amip/).

615 **References**

- 616 Arnold, N. P., and D. A. Randall, 2015: Global-scale convective aggregation: Implications for the
617 Madden-Julian Oscillation. *J. Adv. Model. Earth Sys.*, doi:10.1002/2015MS000498.
- 618 Becker, T., B. Stevens, and C. Hohenegger, 2017: Imprint of the convective parameterization and
619 sea-surface temperature on large-scale convective self-aggregation. *J. Adv. Model. Earth Syst.*,
620 **9**, 1488–1505, doi:10.1002/2016MS000865.
- 621 Bosilovich, M. G., and Coauthors, 2015: MERRA-2: Initial evaluation of the climate. *NASA/TM-*
622 *2015-14606*, Vol. **43**, 139 pp., URL <https://gmao.gsfc.nasa.gov/pubs/docs/Bosilovich803.pdf>.
- 623 Bretherton, C. S., J. R. McCaa, and H. Grier, 2004: A new parameterization for shallow cumu-
624 lus convection and its application to marine subtropical cloud-topped boundary layers. part I:

625 Description and 1D results. *Mon. Weather Rev.*, **132**, 864–882.

626 Bretherton, C. S., and S. Park, 2009: A new moist turbulence parameterization in the Community
627 Atmosphere Model. *Journal of Climate*, **22** (12), 3422–3448, doi:10.1175/2008JCLI2556.1,
628 <https://doi.org/10.1175/2008JCLI2556.1>.

629 Bu, Y., R. Fovell, and K. Corbosiero, 2014: Influence of cloud radiative forcing on tropical cyclone
630 structure. *J. Atmos. Sci.*, **71**, 1644–1662, doi:10.1175/JAS-D-13-0265.1.

631 Bu, Y., R. G. Fovell, and K. L. Corbosiero, 2017: The influences of boundary layer mixing and
632 cloud-radiative forcing on tropical cyclone size. *J. Atmos. Sci.*, doi:10.1175/JAS-D-16-0231.1.

633 Camargo, S., and A. Wing, 2016: Tropical cyclones in climate models. *WIREs Climate Change*,
634 **7**, 211–237, doi:10.1002/wcc373.

635 Camargo, S. J., 2013: Global and regional aspects of tropical cyclone activity in the CMIP5 mod-
636 els. *J. Climate*, **26**, 9880–9902, doi:10.1175/JCLI-D-12-00549.1.

637 Camargo, S. J., and S. E. Zebiak, 2002: Improving the detection and tracking of tropical cyclones
638 in atmospheric general circulation models. *Weather and Forecasting*, **17** (6), 1152–1162.

639 Chen, J.-H., and S.-J. Lin, 2011: The remarkable predictability of inter-annual vari-
640 ability of Atlantic hurricanes during the past decade. *Geophysical Research Letters*,
641 **38** (11), L11 804, doi:10.1029/2011GL047629, [https://agupubs.onlinelibrary.wiley.com/doi/
642 pdf/10.1029/2011GL047629](https://agupubs.onlinelibrary.wiley.com/doi/pdf/10.1029/2011GL047629).

643 Chen, J.-H., and S.-J. Lin, 2013: Seasonal predictions of tropical cyclones using a 25-km-
644 resolution general circulation model. *Journal of Climate*, **26** (2), 380–398, doi:10.1175/
645 JCLI-D-12-00061.1, <https://doi.org/10.1175/JCLI-D-12-00061.1>.

646 Chou, M.-D., and M. J. Suarez, 1994: An efficient thermal infrared radiation parameterization for
647 use in general circulation models. *NASA Tech. Memorandum 104606*, **Vol. 3**.

648 Chou, M.-D., and M. J. Suarez, 1999: A solar radiation parameterization for atmospheric studies.
649 *NASA Tech. Memorandum 104606*, **Vol. 15**.

650 Chu, J.-H., C. Sampson, A. Levine, and E. Fukada, 2002: The Joint Typhoon Warning Center
651 tropical cyclone best-tracks, 1945-2000. *NRL Technical Report*, **NRL/MR/7540-02-16**.

652 Collow, A., M. Bosilovich, and R. Lucchesi, 2018: File specification for M2AMIP products.
653 *GMAO Office Note*, **No. 15 (Version 1.0)**, 45 pp., URL [https://gmao.gsfc.nasa.gov/pubs/docs/
654 Collow1024.pdf](https://gmao.gsfc.nasa.gov/pubs/docs/Collow1024.pdf).

655 Collow, A. B. M., S. P. Mahanama, M. G. Bosilovich, R. D. Koster, and S. D. Schubert, 2017: An
656 evaluation of teleconnections over the United States in an ensemble of AMIP simulations with
657 the MERRA-2 configuration of the GEOS atmospheric model. *NASA/TM-2017-104606*, **47**, 78
658 pp., URL <https://gmao.gsfc.nasa.gov/pubs/docs/Collow963.pdf>.

659 Coppin, D., and S. Bony, 2015: Physical mechanisms controlling the initiation of convective self-
660 aggregation in a General Circulation Model. *Journal of Advances in Modeling Earth Systems*,
661 **7 (4)**, 2060–2078, doi:10.1002/2015MS000571.

662 Delworth, T. L., and Coauthors, 2012: Simulated climate and climate change in the GFDL CM2.5
663 high-resolution coupled climate model. *J. Climate*, **25**, 2755–2781.

664 Dennis, J., and Coauthors, 2012: CAM-SE: A scalable spectral element dynamical core for the
665 Community Atmosphere Model. *Int. J. High Perf. Comput. Appl.*, **26**, 74–89, doi:10.1177/
666 1094342011428142.

667 Duvel, J., S. Camargo, and A. Sobel, 2017: Role of convection scheme in modeling initiation and
668 intensification of tropical depressions over the North Atlantic. *Mon. Wea. Rev.*

669 Fovell, R., Y. P. Bu, K. L. Corbosiero, W. Tung, Y. Cao, H.-C. Kuo, L. Hsu, and H. Su, 2016:
670 Influence of cloud microphysics and radiation on tropical cyclone structure and motion. *Meteo-*
671 *rological Monographs*, **56**, 11.1–11.27, doi:10.1175/AMSMONOGRAPHS-D-15-0006.1.

672 Fovell, R., K. L. Corbosiero, A. Seifert, and K.-N. Liou, 2010: Impact of cloud-radiative processes
673 on hurricane track. *Geophys. Res. Lett.*, **37**, L07 808, doi:10.1029/2010GL042691.

674 Gelaro, R., and Coauthors, 2017: The Modern-Era Retrospective analysis for Research and
675 Applications, version 2 (MERRA-2). *Journal of Climate*, **30** (14), 5419–5454, doi:10.1175/
676 JCLI-D-16-0758.1.

677 GFDL Global Atmospheric Model Development Team, T., 2004: The new GFDL global atmo-
678 sphere and land model AM2-LM2: Evaluation with prescribed SST simulations. *Journal of*
679 *Climate*, **17** (24), 4641–4673, doi:10.1175/JCLI-3223.1, <https://doi.org/10.1175/JCLI-3223.1>.

680 Halperin, D. J., H. E. Fuelberg, R. E. Hart, and J. H. Cossuth, 2016: Verification of tropi-
681 cal cyclone genesis forecasts from global numerical models: Comparisons between the north
682 atlantic and eastern north pacific basins. *Weather and Forecasting*, **31** (3), 947–955, doi:
683 10.1175/WAF-D-15-0157.1.

684 Harris, L. M., S.-J. Lin, and C.-Y. Tu, 2016: High-resolution climate simulations using gfdl
685 hiram with a stretched global grid. *Journal of Climate*, **29** (11), 4293–4314, doi:10.1175/
686 JCLI-D-15-0389.1, <https://doi.org/10.1175/JCLI-D-15-0389.1>.

687 Hohenegger, C., and B. Stevens, 2016: Coupled radiative convective equilibrium simulation-
688 swith explicit and parameterized convection. *J. Adv. Model. Earth Sys.*, **8**, doi:10.1002/
689 2016MS000666.

690 Holloway, C., 2017: Convective aggregation in realistic convective-scale simulations. *J. Adv.*
691 *Model. Earth Syst.*, **9**, 1450–1472, doi:10.1002/2017MS000980.

692 Holloway, C. E., and S. J. Woolnough, 2016: The sensitivity of convective aggregation to dia-
693 batic processes in idealized radiative-convective equilibrium simulations. *Journal of Advances*
694 *in Modeling Earth Systems*, **8 (1)**, 166–195, doi:10.1002/2015MS000511.

695 Hurrell, J. W., J. J. Hack, D. Shea, J. M. Caron, and J. Rosinski, 2008: A new sea surface temper-
696 ature and sea ice boundary dataset for the Community Atmosphere Model. *Journal of Climate*,
697 **21 (19)**, 5145–5153, doi:10.1175/2008JCLI2292.1.

698 Kim, D., A. H. Sobel, A. D. D. Genio, Y. Chen, S. J. Camargo, M.-S. Yao, M. Kelley, and
699 L. Nazarenko, 2012: The tropical subseasonal variability simulated in the NASA GISS gen-
700 eral circulation model. *J. Climate*, **25**, 4641–4659.

701 Kim, D., and Coauthors, 2018: Process-oriented diagnosis of tropical cyclones in high-resolution
702 GCMs. *J. Climate*, **31**, 1685–1702, doi:10.1175/JCLI-D-17-0269.1.

703 Knutson, T. R., J. J. Sirutis, S. T. Garner, I. M. Held, and R. E. Tuleya, 2007: Simulation of the
704 recent multidecadal increase of Atlantic hurricane activity using an 18-km-grid regional model.
705 *Bull. Amer. Meteor. Soc.*, **88**, 1549–1565.

706 Landsea, C., and J. Franklin, 2013: Atlantic hurricane database uncertainty and presentation of
707 new database format. *Mon. Wea. Rev.*, **141**, 3576–3592.

708 Lee, C.-Y., M. Tippett, A. Sobel, and S. Camargo, 2016: Rapid intensification and the bimodal
709 distribution of tropical cyclone intensity. *Nature Communications*, doi:10.1038/ncomms10625.

710 Lim, Y.-K., S. D. Schubert, O. Reale, M.-I. Lee, A. M. Molod, and M. J. Suarez, 2015: Sensitivity
711 of tropical cyclones to parameterized convection in the NASA GEOS-5 model. *J. Climate*, **28**,
712 551–573.

713 Lin, S.-J., and R. B. Rood, 1996: Multidimensional flux-form semi-lagrangian transport schemes.
714 *Monthly Weather Review*, **124 (9)**, 2046–2070.

715 Lin, S.-J., and R. B. Rood, 1997: An explicit flux-form semi-lagrangian shallow-water model
716 on the sphere. *Quarterly Journal of the Royal Meteorological Society*, **123 (544)**, 2477–2498,
717 doi:10.1002/qj.49712354416.

718 Lloyd, I. D., and G. A. Vecchi, 2011: Observational evidence for oceanic controls on hurricane
719 intensity. *Journal of Climate*, **24 (4)**, 1138–1153, doi:10.1175/2010JCLI3763.1, [https://doi.org/](https://doi.org/10.1175/2010JCLI3763.1)
720 [10.1175/2010JCLI3763.1](https://doi.org/10.1175/2010JCLI3763.1).

721 Manganello, J., and Coauthors, 2012: Tropical cyclone climatology in a 10-km global atmospheric
722 GCM: Toward weather-resolving climate modeling. *J. Climate*, **25**, 3867–3893.

723 Melhauser, C., and F. Zhang, 2014: Diurnal radiation cycle impact on the pregenesis environment
724 of Hurricane Karl (2010). *J. Atmos. Sci.*, **71**, 1242–1259, doi:10.1175/JAS-D-13-0116.1.

725 Mlawer, E. J., T. S. J., B. P. D., I. M. J., and C. S. A., 1997: Radiative transfer for inhomogeneous
726 atmospheres: RRTM, a validated correlated-k model for the longwave. *Journal of Geophysical*
727 *Research: Atmospheres*, **102 (D14)**, 16 663–16 682, doi:10.1029/97JD00237.

- 728 Molod, A., L. Takacs, M. Suarez, and J. Bacmeister, 2015: Development of the GEOS-5 atmo-
729 spheric general circulation model: Evolution from MERRA to MERRA2. *Geoscientific Model*
730 *Development*, **8 (5)**, 1339–1356, doi:10.5194/gmd-8-1339-2015.
- 731 Moon, Y., and Coauthors, 2018: Exploring the effect of horizontal resolution on tropical cyclone
732 structures and intensity in global climate model simulations. *J. Climate*, **in prep.**
- 733 Moorthi, S., and M. J. Suarez, 1992: Relaxed Arakawa-Schubert: A parameterization of moist
734 convection for general circulation models. *Mon. Weather Rev.*, **120**, 978–1002.
- 735 Muller, C. J., and D. M. Romps, 2018: Acceleration of tropical cyclogenesis by self-aggregation
736 feedbacks. *Proceedings of the National Academy of Sciences*, doi:10.1073/pnas.1719967115.
- 737 Murakami, H., G. Villarini, G. A. Vecchi, W. Zhang, and R. Gudgel, 2016: Statistical-dynamical
738 seasonal forecast of North Atlantic and U.S. landfalling tropical cyclones using the high-
739 resolution GFDL FLOR coupled models. *Monthly Weather Review*, **144 (6)**, 2101–2123, doi:
740 10.1175/MWR-D-15-0308.1.
- 741 Murakami, H., and Coauthors, 2012: Future changes in tropical cyclone activity projected by the
742 new high-resolution MRI-AGCM. *J. Climate*, **25**, 3237–3260, doi:10.1175/JCLI-D-11-00415.
743 1.
- 744 Murakami, H., and Coauthors, 2015: Simulation and prediction of category 4 and 5 hurricanes
745 in the high-resolution GFDL HiFLOR coupled climate models. *Journal of Climate*, **28 (23)**,
746 9058–9079, doi:10.1175/JCLI-D-15-0216.1.
- 747 Navarro, E. L., and G. J. Hakim, 2016: Idealized numerical modeling of the diurnal cycle of
748 tropical cyclones. *J. Atmos. Sci.*, **73**, 4189–4201, doi:10.1175/JAS-D-15-0349.1.

- 749 Neale, R., and Coauthors, 2012: Description of the NCAR Community Atmosphere Model
750 (CAM 5.0). *NCAR Tech. Note TN-486*, URL [http://www.cesm.ucar.edu/models/cesm1.0/cam/](http://www.cesm.ucar.edu/models/cesm1.0/cam/docs/description/cam5_desc.pdf)
751 [docs/description/cam5_desc.pdf](http://www.cesm.ucar.edu/models/cesm1.0/cam/docs/description/cam5_desc.pdf).
- 752 Nicholls, M. E., 2015: An investigation of how radiation may cause accelerated rates of tropical
753 cyclogenesis and diurnal cycles of convective activity. *Atmospheric Chemistry and Physics*,
754 **15** (15), 9003–9029, doi:10.5194/acp-15-9003-2015.
- 755 O’Neill, M., D. Perez-Betancourt, and A. A. Wing, 2017: Accessible environments for diurnal-
756 period waves in simulated tropical cyclones. *J. Atmos. Sci.*, **74**, 2489–2505, doi:10.1175/
757 JAS-D-16-0294.1.
- 758 Park, S., and C. S. Bretherton, 2009: The University of Washington shallow convection and moist
759 turbulence schemes and their impact on climate simulations with the Community Atmosphere
760 Model. *Journal of Climate*, **22** (12), 3449–3469, doi:10.1175/2008JCLI2557.1.
- 761 Putman, W., and S.-J. Lin, 2007: Finite-volume transport on various cubed-sphere grids. *J. Com-
762 put. Phys.*, **64**, 3377–3405.
- 763 Rayner, N. A., D. E. Parker, E. B. Horton, C. K. Folland, L. V. Alexander, , and D. P. Rowell, 2003:
764 Global analysis of sea surface temperature, sea ice, and night marine air temperature since the
765 late nineteenth century. *J. Geophys. Res.*, **108**, 4407, doi:10.1029/2002JD002670.
- 766 Reed, K. A., and C. Jablonowski, 2011: Impact of physical parameterizations on idealized tropical
767 cyclones in the Community Atmosphere Model. *Geophys. Res. Lett.*, **38**.
- 768 Reed, K. A., and Coauthors, 2015: Impact of the dynamical core on the direct simulation of
769 tropical cyclones in a high-resolution global model. *Geophys. Res. Lett.*, **42**, 3603–3608.

770 Rienecker, M., and Coauthors, 2008: The GEOS-5 data assimilation system, documentation of
771 versions 5.0.1, 5.1.0, and 5.2.0. *NASA/TM-2008-104606*, **Vol. 27**, 101 pp., URL [https://gmao.
772 gsfc.nasa.gov/pubs/docs/Rienecker369.pdf](https://gmao.gsfc.nasa.gov/pubs/docs/Rienecker369.pdf).

773 Roberts, M., and Coauthors, 2015: Tropical cyclones in the upscale ensemble of high-resolution
774 global climate models. *J. Climate*, **28**, 574–596, doi:10.1175/JCLI-D-14-00131.1.

775 Scoccimarro, E., P. Fogli, K. Reed, S. Gualdi, S. Masina, and A. Navarra, 2017: Tropical cyclone
776 interaction with the ocean: The role of high-frequency (subdaily) coupled processes. *J. Climate*,
777 **30**, 145–162, doi:10.1175/JCLI-D-16-0292.1.

778 Shaevitz, D. A., and Coauthors, 2014: Characteristics of tropical cyclones in high-resolution mod-
779 els in the present climate. *J. Adv. Model. Earth Syst.*, **6**, 1154–1172.

780 Tang, X., and F. Zhang, 2016: Impacts of the diurnal radiation cycle on the formation, intensity,
781 and structure of Hurricane Edouard (2014). *Journal of the Atmospheric Sciences*, **73 (7)**, 2871–
782 2892, doi:10.1175/JAS-D-15-0283.1.

783 Ullrich, P. A., and C. M. Zarzycki, 2017: TempestExtremes: A framework for scale-insensitive
784 pointwise feature tracking on unstructured grids. *Geoscientific Model Development*, **10 (3)**,
785 1069–1090, doi:10.5194/gmd-10-1069-2017.

786 Vecchi, G. A., and Coauthors, 2014: On the seasonal forecasting of regional tropical cyclone
787 activity. *J. Climate*, **27**, 7994–8016.

788 Vitart, F., D. Anderson, and T. Stockdale, 2003: Seasonal forecasting of tropical cyclone landfall
789 over Mozambique. *J. Climate*, **16**, 3932–3945.

790 Vitart, F., J. L. Anderson, and W. F. Stern, 1997: Simulation of interannual variability of tropical
791 storm frequency in an ensemble of GCM integrations. *J. Climate*, **10**, 745–760.

- 792 Vitart, F., A. Leroy, and M. C. Wheeler, 2010: A comparison of dynamical and statistical predic-
793 tions of weekly tropical cyclone activity in the southern hemisphere. *Monthly Weather Review*,
794 **138** (9), 3671–3682, doi:10.1175/2010MWR3343.1.
- 795 Walsh, K., and coauthors, 2016: Tropical cyclones and climate change. *WIREs Clim. Change*, **7**,
796 65–89.
- 797 Wehner, M. F., and Coauthors, 2014: The effect of horizontal resolution on simulation quality in
798 the Community Atmospheric Model, CAM5.1. *Journal of Advances in Modeling Earth Systems*,
799 **6** (4), 980–997, doi:10.1002/2013MS000276.
- 800 Wing, A. A., S. J. Camargo, and A. H. Sobel, 2016: Role of radiative-convective feedbacks in
801 spontaneous tropical cyclogenesis in idealized numerical simulations. *Journal of the Atmo-*
802 *spheric Sciences*, **73**, 2633–2642, doi:10.1175/JAS-D-15-0380.1.
- 803 Wing, A. A., and T. W. Cronin, 2016: Self-aggregation of convection in long channel geometry.
804 *Q. J. R. Meteorol. Soc.*, **142**, 1–15, doi:10.1002/qj.2628.
- 805 Wing, A. A., and K. A. Emanuel, 2014: Physical mechanisms controlling self-aggregation of
806 convection in idealized numerical modeling simulations. *J. Adv. Model. Earth Syst.*, **6**, 59–74,
807 doi:10.1002/2013MS000269.
- 808 Zarzycki, C., 2016: Tropical cyclone intensity errors associated with lack of two-way ocean
809 coupling in high-resolution global simulations. *J. Climate*, **29**, 8589–8610, doi:10.1175/
810 JCLI-D-16-0273.1.
- 811 Zarzycki, C. M., M. N. Levy, C. Jablonowski, J. R. Overfelt, M. A. Taylor, and P. A. Ullrich, 2014:
812 Aquaplanet experiments using CAM’s variable-resolution dynamical core. *Journal of Climate*,
813 **27** (14), 5481–5503, doi:10.1175/JCLI-D-14-00004.1.

- 814 Zarzycki, C. M., K. A. Reed, J. T. Bacmeister, A. P. Craig, S. C. Bates, and N. A. Rosenbloom,
815 2016: Impact of surface coupling grids on tropical cyclone extremes in high-resolution atmo-
816 spheric simulations. *Geosci. Model Dev.*, doi:10.5194/gmd-9-779-2016.
- 817 Zarzycki, C. M., D. R. Thatcher, and C. Jablonowski, 2017: Objective tropical cyclone extra-
818 tropical transition detection in high-resolution reanalysis and climate model data. *Journal of*
819 *Advances in Modeling Earth Systems*, **9** (1), 130–148, doi:10.1002/2016MS000775.
- 820 Zhang, G., and N. A. McFarlane, 1995: Sensitivity of climate simulations to the parameterization
821 of cumulus convection in the Canadian climate centre general circulation model. *Atmosphere-*
822 *Ocean*, **33** (3), 407–446, doi:10.1080/07055900.1995.9649539.
- 823 Zhang, W., and Coauthors, 2016: Improved simulation of tropical cyclone responses to ENSO in
824 the western North Pacific in the high-resolution GFDL HiFLOR coupled climate model. *Journal*
825 *of Climate*, **29** (4), 1391–1415, doi:10.1175/JCLI-D-15-0475.1.
- 826 Zhao, M., I. M. Held, S.-J. Lin, and G. A. Vecchi, 2009: Simulations of global hurricane clima-
827 tology, interannual variability, and response to global warming using a 50-km resolution gcm.
828 *J. Climate*, **22**, 6653–6678.
- 829 Zhao, M., I. M. Held, S.-J. Lin, and G. A. Vecchi, 2012: Some counterintuitive dependencies of
830 tropical cyclone frequency on parameters in a GCM. *J. Atmos. Sci.*, **69**, 2272–2283.

831 **LIST OF TABLES**

832 **Table 1.** Description of model simulations. 40

833 **Table 2.** Number of tropical cyclones (TCs) analyzed. Only TCs in the North Atlantic
834 are analyzed in CAM-SE. 41

835 **Table 3.** TC intensity bins and number of snapshots per bin 42

TABLE 1. Description of model simulations.

| Model | Resolution | Dynamical Core | Convection Scheme | Other Notes |
|--------|---------------------------------------|----------------------------------|--|--|
| HiRAM | ~ 50 km | Finite volume cubed sphere | Bretherton et al. (2004) | Other physics: GFDL AM2 |
| AM2.5 | ~ 50 km | Finite volume cubed sphere | Relaxed Arakawa-Schubert | Other physics: GFDL AM2 |
| FLOR | ~ 50 km | Finite volume cubed sphere | Relaxed Arakawa-Schubert | Coupled to 1° ocean, SST nudged to obs. |
| CAM-FV | ~ 25 km | Finite volume latitude-longitude | Park and Bretherton (2009) shallow, Zhang and McFarlane (1995) deep | NCAR/DOE CAM5 |
| CAM-SE | ~ 25 km in N. Atl. ~ 100 km global | Spectral element | Park and Bretherton (2009) shallow, Zhang and McFarlane (1995) deep | NCAR/DOE CAM5 |
| GEOS | ~ 50 km | Finite volume cubed sphere | Relaxed Arakawa-Schubert | MERRA-2 AMIP |

836 TABLE 2. Number of tropical cyclones (TCs) analyzed. Only TCs in the North Atlantic are analyzed in
837 CAM-SE.

| Model | Years Analyzed | Number of TCs |
|--------|----------------|---------------|
| HiRAM | 1984-1985 | 203 |
| AM2.5 | 1984-1985 | 170 |
| FLOR | 1984-1985 | 211 |
| CAM-FV | 1996-1997 | 146 |
| CAM-SE | 1992-1999 | 91 |
| GEOS | 1984-1985 | 84 |

TABLE 3. TC intensity bins and number of snapshots per bin

| Bin | Intensity Range (ms^{-1}) | HiRAM | AM2.5 | FLOR | CAM-FV | CAM-SE | GEOS |
|-----|--------------------------------------|-------|-------|------|--------|--------|------|
| 1 | $6 \leq V_m < 9$ | 0 | 4 | 5 | 0 | 3 | 254 |
| 2 | $9 \leq V_m < 12$ | 0 | 142 | 154 | 1 | 15 | 504 |
| 3 | $12 \leq V_m < 15$ | 41 | 413 | 512 | 25 | 72 | 721 |
| 4 | $15 \leq V_m < 18$ | 431 | 628 | 736 | 246 | 131 | 944 |
| 5 | $18 \leq V_m < 21$ | 630 | 667 | 994 | 673 | 173 | 524 |
| 6 | $21 \leq V_m < 24$ | 540 | 645 | 884 | 935 | 184 | 247 |
| 7 | $24 \leq V_m < 27$ | 440 | 435 | 543 | 808 | 154 | 110 |
| 8 | $27 \leq V_m < 30$ | 306 | 266 | 256 | 604 | 119 | 74 |
| 9 | $30 \leq V_m < 33$ | 236 | 145 | 126 | 488 | 88 | 23 |
| 10 | $33 \leq V_m < 35$ | 92 | 49 | 47 | 232 | 59 | 9 |
| 11 | $35 \leq V_m < 38$ | 125 | 20 | 24 | 272 | 60 | 12 |
| 12 | $38 \leq V_m < 41$ | 102 | 8 | 3 | 239 | 45 | 3 |
| 13 | $41 \leq V_m < 44$ | 84 | 3 | 4 | 167 | 49 | 0 |
| 14 | $44 \leq V_m < 47$ | 43 | 4 | 0 | 102 | 31 | 0 |
| 15 | $47 \leq V_m < 50$ | 9 | 0 | 0 | 101 | 32 | 0 |

838 **LIST OF FIGURES**

839 **Fig. 1.** Genesis positions for tropical cyclones in each model (a-f) and in the best-track observa-
840 tional data (g), for 1995-2000. For the models, the genesis position is the latitude and
841 longitude of the first point in the track, as determined by the tracking algorithm. 45

842 **Fig. 2.** Probability density function of lifetime maximum intensity (LMI) (a) and of the maximum
843 wind speed at each snapshot along the TC track up until the time of LMI (b), for the two
844 years of TCs that are analyzed in each model, excluding snapshots poleward of 30° and, in
845 CAM-SE, excluding storms outside of the North Atlantic. “HiRAM-G” (in cyan) indicates
846 TCs in the HiRAM simulation that have been identified and tracked using the GFDL tracking
847 algorithm (the same as used for AM2.5 and FLOR; Murakami et al. 2015). The black dashed
848 line in (a) shows the observed distribution of LMI from the best-track data, for storms of at
849 least tropical storm strength ($LMI \geq 17 \text{ ms}^{-1}$) from 1995-2000, and equatorward of 30°. The PDF in (a) is smoothed while the PDF in (b) uses the un-smoothed 3 ms^{-1} bins from
850 Table 3 (extended to 93 ms^{-1}). 46

852 **Fig. 3.** Composite 48 hours prior to LMI of moist static energy budget (MSE) of all TCs in CAM-
853 FV. The composite mean TC intensity (blue line) and number of storms in the composite
854 (red line) as a function of time relative to LMI is shown in (a); the star indicates the time at
855 which the rest of the panels are valid. The column-integrated MSE (b), MSE tendency (c),
856 column radiative flux convergence (d), surface enthalpy flux (SEF) (e) and MSE advection
857 (f) are also shown as a function of latitude and longitude relative to the TC center. 47

858 **Fig. 4.** Composite 48 hours prior to LMI of moist static energy variance (MSE) budget in CAM-FV.
859 The composite mean TC intensity (blue line) and number of storms in the composite (red
860 line) as a function of time relative to LMI is shown in (a); the star indicates the time at which
861 the rest of the panels are valid. The column-integrated MSE anomaly from the box mean (b),
862 MSE variance tendency (c), radiative feedback (d), surface flux feedback (e) and advective
863 feedback (f) are also shown as a function of latitude and longitude relative to the TC center. 48

864 **Fig. 5.** Composite 96 hours prior to LMI of radiative (g-l) and surface flux feedbacks (m-r) as a
865 function of latitude and longitude relative to the TC center in the CAM-SE (a,g,m), CAM-
866 FV (b,h,n), HiRAM (c,i,o), AM2.5 (d,j,p), FLOR (e,k,q), and GEOS (f,l,r) simulations. The
867 composite mean TC intensity as a function of time relative to LMI is shown in the first row
868 (a-f); the star indicates the time at which the rest of the panels are valid. 49

869 **Fig. 6.** As in Fig. 5 but for composite 72 hours prior to LMI. 50

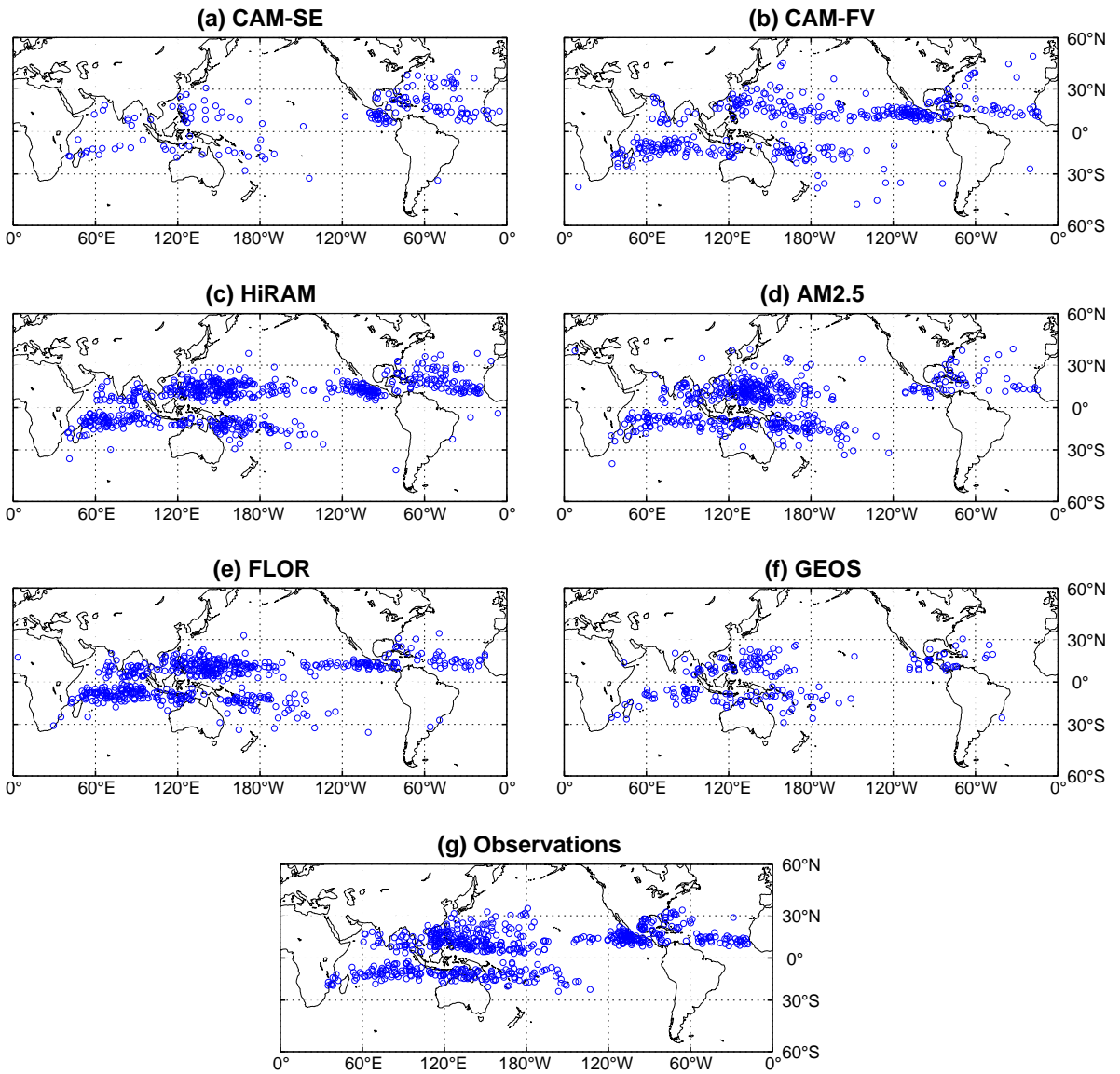
870 **Fig. 7.** As in Fig. 5 but for composite 48 hours prior to LMI. 51

871 **Fig. 8.** As in Fig. 5 but for composite 24 hours prior to LMI. 52

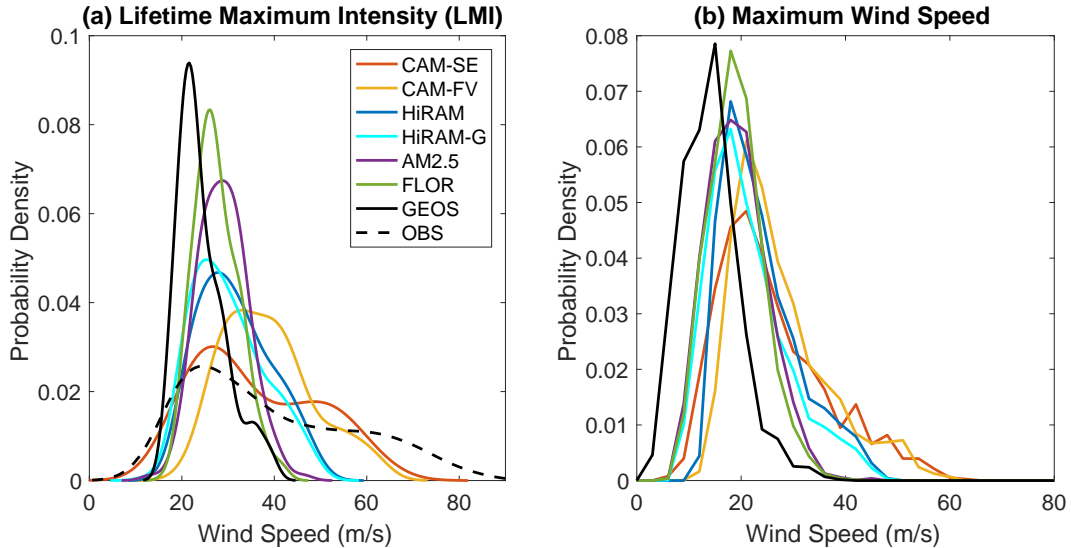
872 **Fig. 9.** Composite 48 hours prior to LMI of normalized radiative (g-l) and surface flux feedbacks
873 (m-r) as a function of latitude and longitude relative to the TC center in the CAM-SE (a,g,m),
874 CAM-FV (b,h,n), HiRAM (c,i,o), AM2.5 (d,j,p), FLOR (e,k,q), and GEOS (f,l,r) simula-
875 tions. The composite mean TC intensity as a function of time relative to LMI is shown in
876 the first row (a-f); the star indicates the time at which the rest of the panels are valid. 53

877 **Fig. 10.** Composite of the box-average MSE variance budget in the CAM-SE (a,g), CAM-FV (b,h),
878 HiRAM (c,i), AM2.5 (d,j), FLOR (e,k), and GEOS (f,l) simulations. The first row (a-f)
879 shows, as a function of time relative to LMI, the composite mean TC intensity (red line, right
880 axis) and the box-average MSE variance (blue line, left axis), scaled by 10^{14} . The second

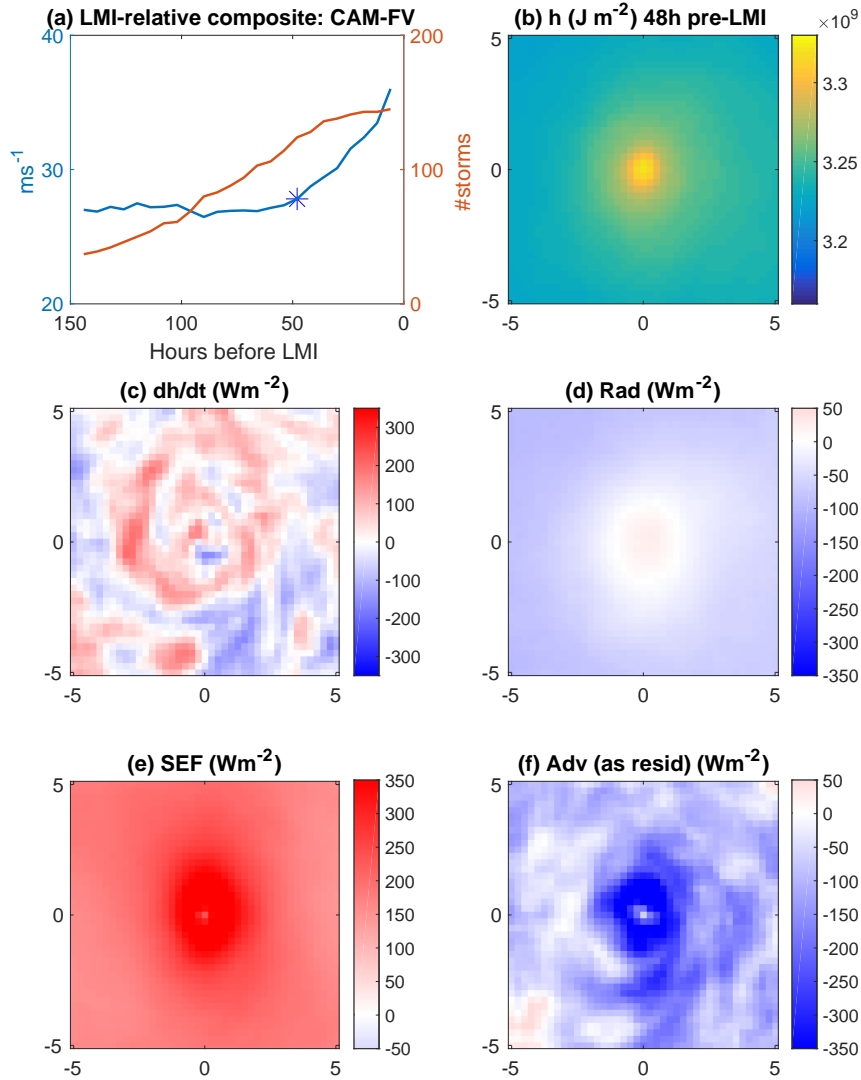
| | | |
|-----|--|----|
| 881 | row (g-l) shows, as a function of time relative to LMI, the surface flux (green line), longwave | |
| 882 | (blue line), shortwave (red line), and advective (pink line) feedbacks. The composite is over | |
| 883 | all TCs that have a LMI in the upper quartile of the LMI distribution. | 54 |
| 884 | Fig. 11. Panel (a) shows the composite of the box-average surface flux (asterisks) and longwave | |
| 885 | radiative feedback (open circles) at 48 hours prior to LMI for each model as a function of | |
| 886 | that models TC intensity. Panel (b) shows the ratio of the composite box-average surface flux | |
| 887 | and radiative feedbacks for each model. Simulated TC intensity is defined as the average | |
| 888 | LMI of all TCs that have LMI in the upper quartile of the LMI distribution. In all panels, | |
| 889 | the models are CAM-SE (red), CAM-FV (yellow), HiRAM (blue), AM2.5 (purple), FLOR | |
| 890 | (green) and GEOS (black). The composite is over all TCs that have a LMI in the upper | |
| 891 | quartile of the LMI distribution. | 55 |
| 892 | Fig. 12. Composite of MSE (Jm^{-2} ; a-f), column radiative flux convergence (g-l) and surface fluxes | |
| 893 | (m-r) as a function of latitude and longitude relative to the TC center in the 24-27 ms^{-1} | |
| 894 | intensity bin, in CAM-SE (a,g,m), CAM-FV (b,h,n), HiRAM (c,i,o), AM2.5 (d,j,p), FLOR | |
| 895 | (e,k,q), and GEOS (f,l,r). | 56 |
| 896 | Fig. 13. Composite of MSE variance (J^2m^{-4} ; a-f), radiative (g-l) and surface flux feedbacks (m-r) | |
| 897 | as a function of latitude and longitude relative to the TC center in the 15-18 ms^{-1} intensity | |
| 898 | bin, in CAM-SE (a,g,m), CAM-FV (b,h,n), HiRAM (c,i,o), AM2.5 (d,j,p), FLOR (e,k,q), | |
| 899 | and GEOS (f,l,r). | 57 |
| 900 | Fig. 14. As in Fig. 13 but for the 24-27 ms^{-1} intensity bin. | 58 |
| 901 | Fig. 15. As in Fig. 13 but for the 33-35 ms^{-1} intensity bin. | 59 |
| 902 | Fig. 16. Composite of normalized MSE variance (a-f), radiative (g-l) and surface flux feedbacks (m- | |
| 903 | r) as a function of latitude and longitude relative to the TC center in the 24-27 ms^{-1} intensity | |
| 904 | bin, in CAM-SE (a,g,m), CAM-FV (b,h,n), HiRAM (c,i,o), AM2.5 (d,j,p), FLOR (e,k,q), | |
| 905 | and GEOS (f,l,r). | 60 |
| 906 | Fig. 17. Box-average MSE variance (a) and surface flux (b) and radiative (c) feedback terms in the | |
| 907 | MSE variance budget composited over intensity bins. The x-axis indicates the mean wind | |
| 908 | speed in each bin, for each model. Panel (c) shows the box-average surface flux (asterisk) | |
| 909 | and radiative (open circle) feedback terms composited over the 24-27 ms^{-1} bin (indicated | |
| 910 | by the dashed line in (b) and (c)) for each model, as a function of the mean LMI of simulated | |
| 911 | TCs in that model. | 61 |



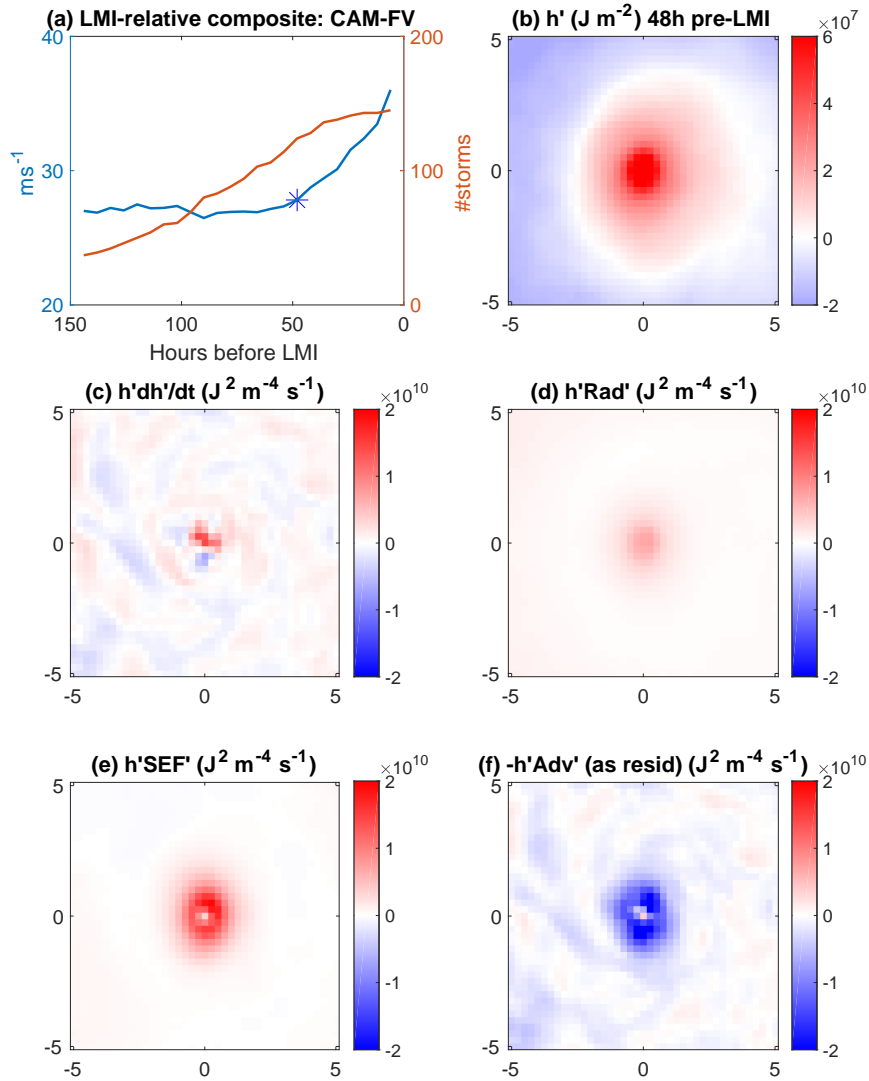
912 FIG. 1. Genesis positions for tropical cyclones in each model (a-f) and in the best-track observational data (g),
 913 for 1995-2000. For the models, the genesis position is the latitude and longitude of the first point in the track, as
 914 determined by the tracking algorithm.



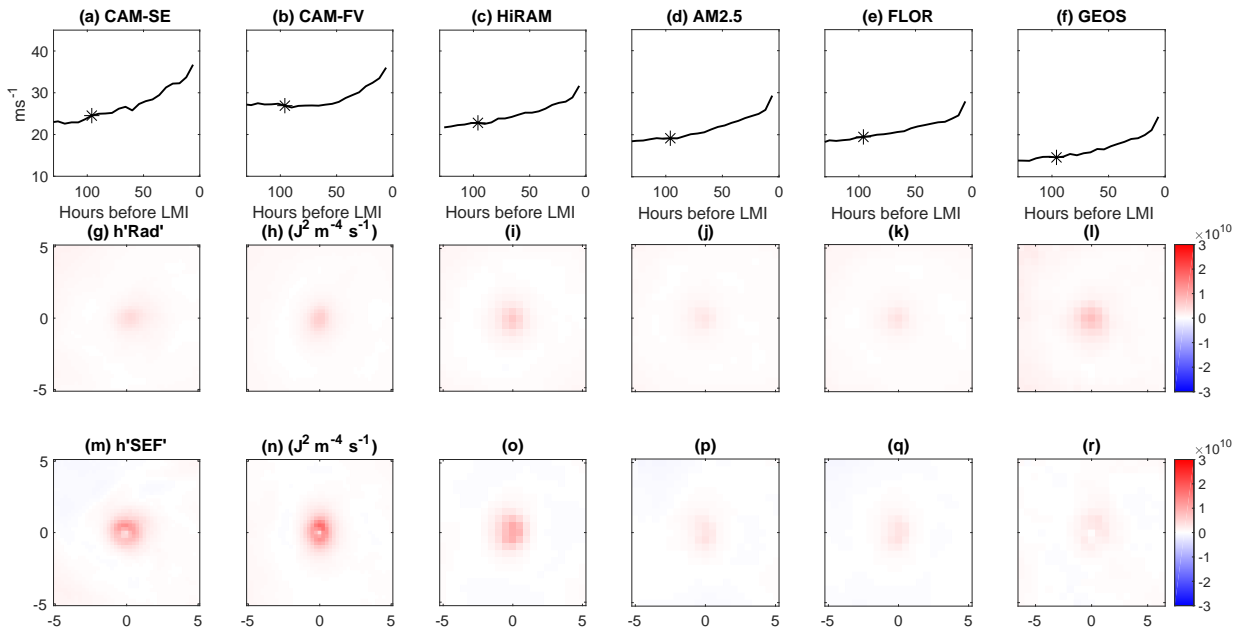
915 FIG. 2. Probability density function of lifetime maximum intensity (LMI) (a) and of the maximum wind speed
 916 at each snapshot along the TC track up until the time of LMI (b), for the two years of TCs that are analyzed
 917 in each model, excluding snapshots poleward of 30° and, in CAM-SE, excluding storms outside of the North
 918 Atlantic. “HiRAM-G” (in cyan) indicates TCs in the HiRAM simulation that have been identified and tracked
 919 using the GFDL tracking algorithm (the same as used for AM2.5 and FLOR; Murakami et al. 2015). The black
 920 dashed line in (a) shows the observed distribution of LMI from the best-track data, for storms of at least tropical
 921 storm strength ($LMI \geq 17 \text{ ms}^{-1}$) from 1995-2000, and equatorward of 30° . The PDF in (a) is smoothed while
 922 the PDF in (b) uses the un-smoothed 3 ms^{-1} bins from Table 3 (extended to 93 ms^{-1}).



923 FIG. 3. Composite 48 hours prior to LMI of moist static energy budget (MSE) of all TCs in CAM-FV. The
 924 composite mean TC intensity (blue line) and number of storms in the composite (red line) as a function of time
 925 relative to LMI is shown in (a); the star indicates the time at which the rest of the panels are valid. The column-
 926 integrated MSE (b), MSE tendency (c), column radiative flux convergence (d), surface enthalpy flux (SEF) (e)
 927 and MSE advection (f) are also shown as a function of latitude and longitude relative to the TC center.



928 FIG. 4. Composite 48 hours prior to LMI of moist static energy variance (MSE) budget in CAM-FV. The
 929 composite mean TC intensity (blue line) and number of storms in the composite (red line) as a function of time
 930 relative to LMI is shown in (a); the star indicates the time at which the rest of the panels are valid. The column-
 931 integrated MSE anomaly from the box mean (b), MSE variance tendency (c), radiative feedback (d), surface flux
 932 feedback (e) and advective feedback (f) are also shown as a function of latitude and longitude relative to the TC
 933 center.



934 FIG. 5. Composite 96 hours prior to LMI of radiative (g-l) and surface flux feedbacks (m-r) as a function
 935 of latitude and longitude relative to the TC center in the CAM-SE (a,g,m), CAM-FV (b,h,n), HiRAM (c,i,o),
 936 AM2.5 (d,j,p), FLOR (e,k,q), and GEOS (f,l,r) simulations. The composite mean TC intensity as a function of
 937 time relative to LMI is shown in the first row (a-f); the star indicates the time at which the rest of the panels are
 938 valid.

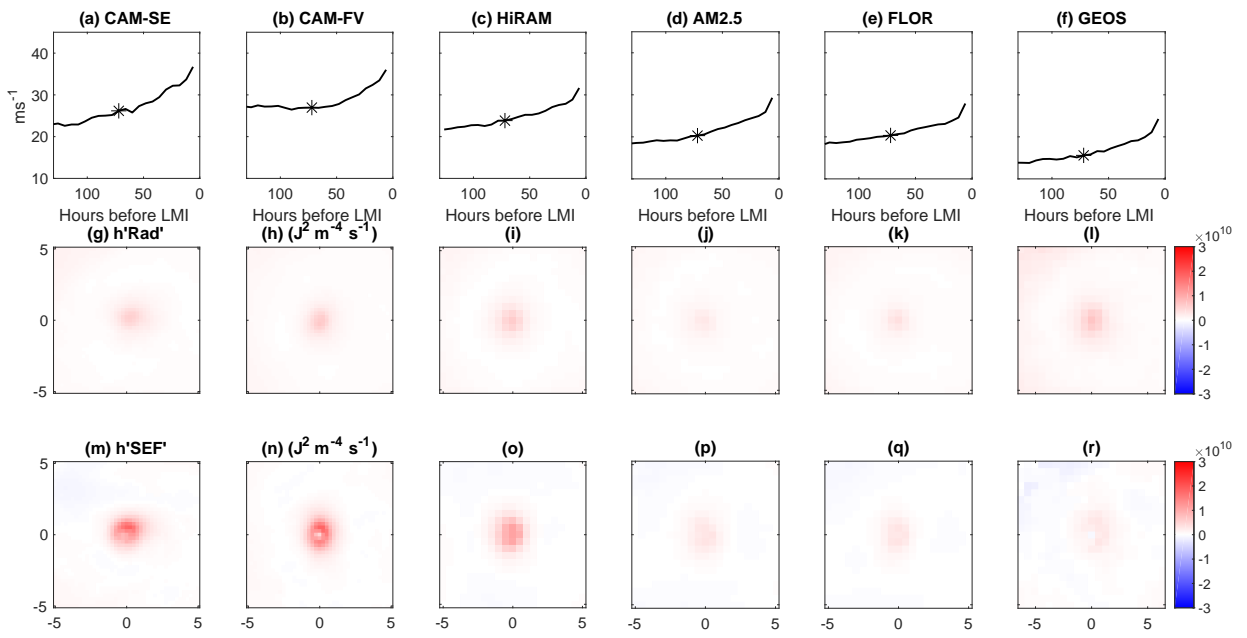


FIG. 6. As in Fig. 5 but for composite 72 hours prior to LMI.

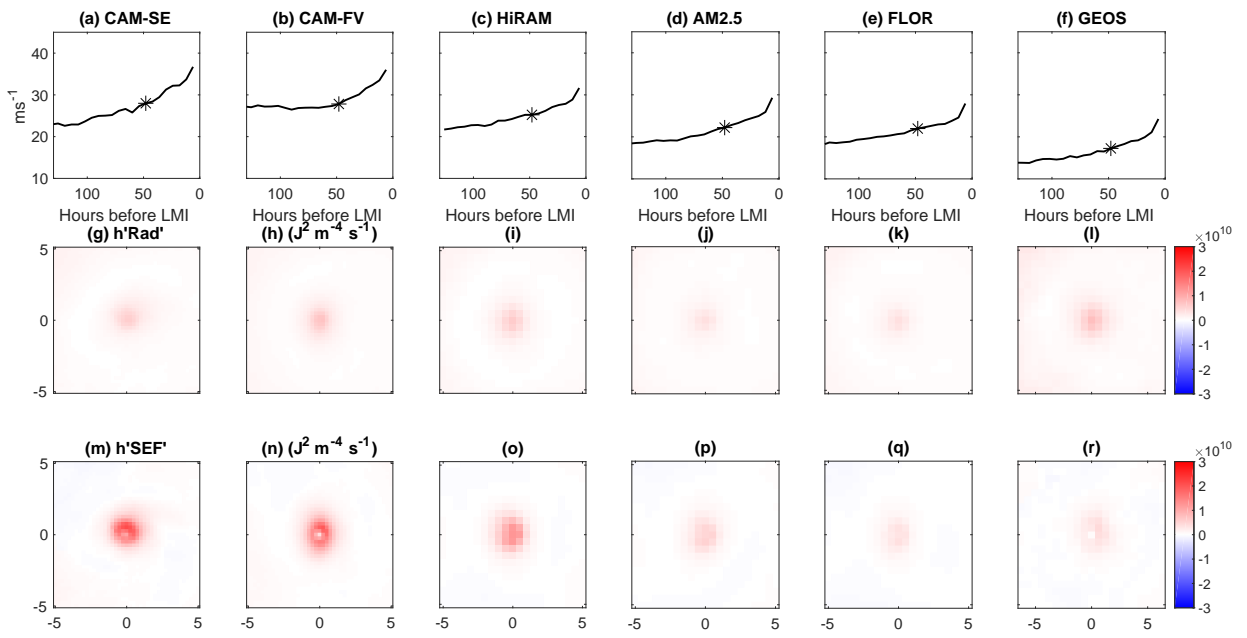


FIG. 7. As in Fig. 5 but for composite 48 hours prior to LMI.

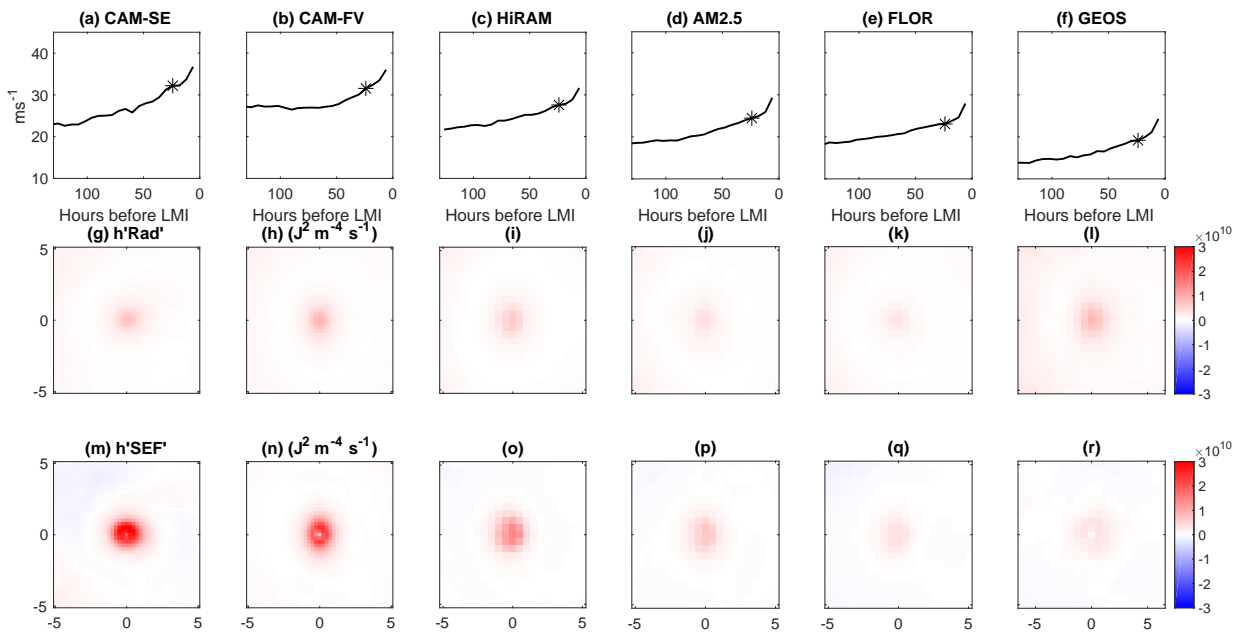
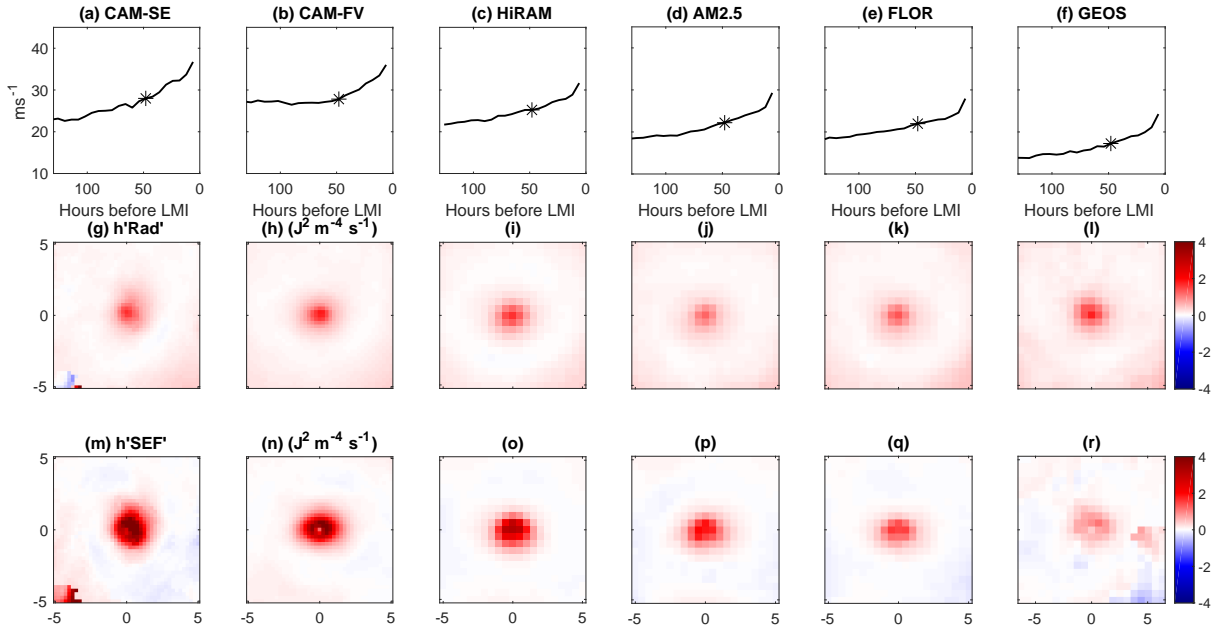
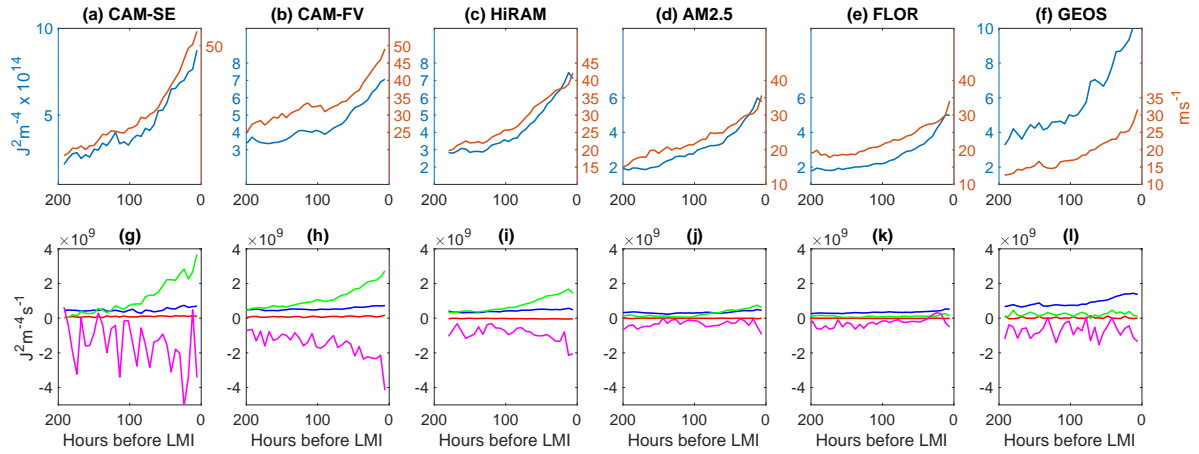


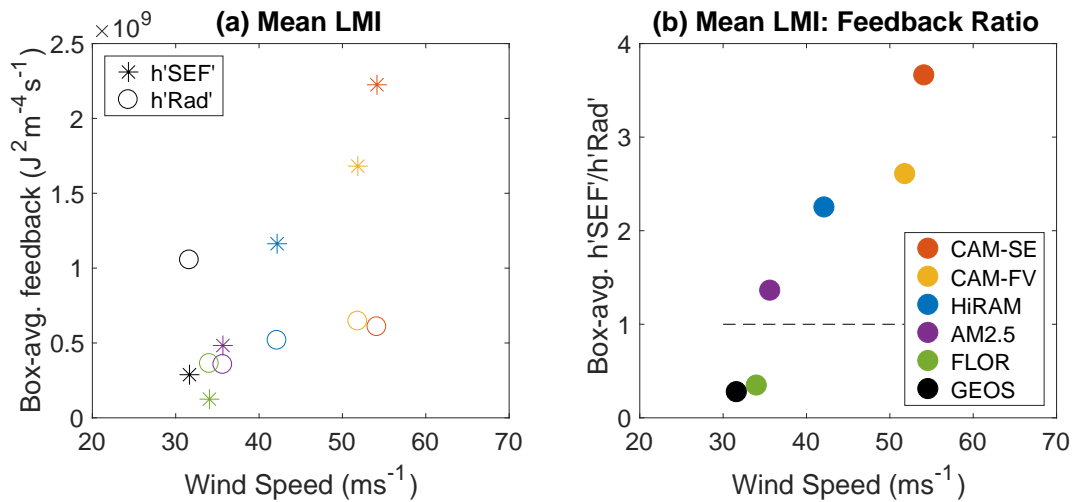
FIG. 8. As in Fig. 5 but for composite 24 hours prior to LMI.



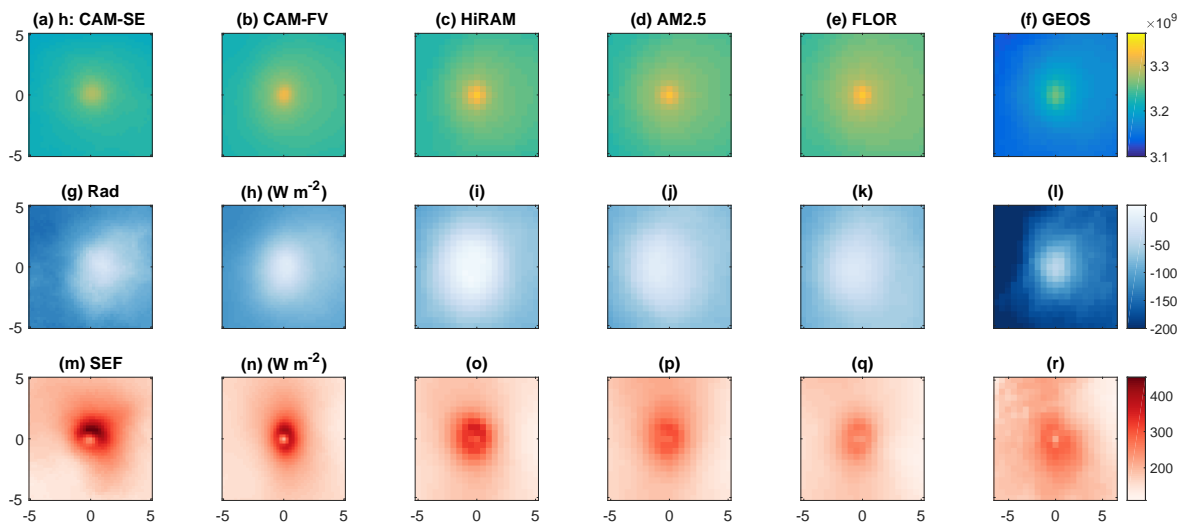
939 FIG. 9. Composite 48 hours prior to LMI of normalized radiative (g-l) and surface flux feedbacks (m-r) as a
 940 function of latitude and longitude relative to the TC center in the CAM-SE (a,g,m), CAM-FV (b,h,n), HiRAM
 941 (c,i,o), AM2.5 (d,j,p), FLOR (e,k,q), and GEOS (f,l,r) simulations. The composite mean TC intensity as a
 942 function of time relative to LMI is shown in the first row (a-f); the star indicates the time at which the rest of the
 943 panels are valid.



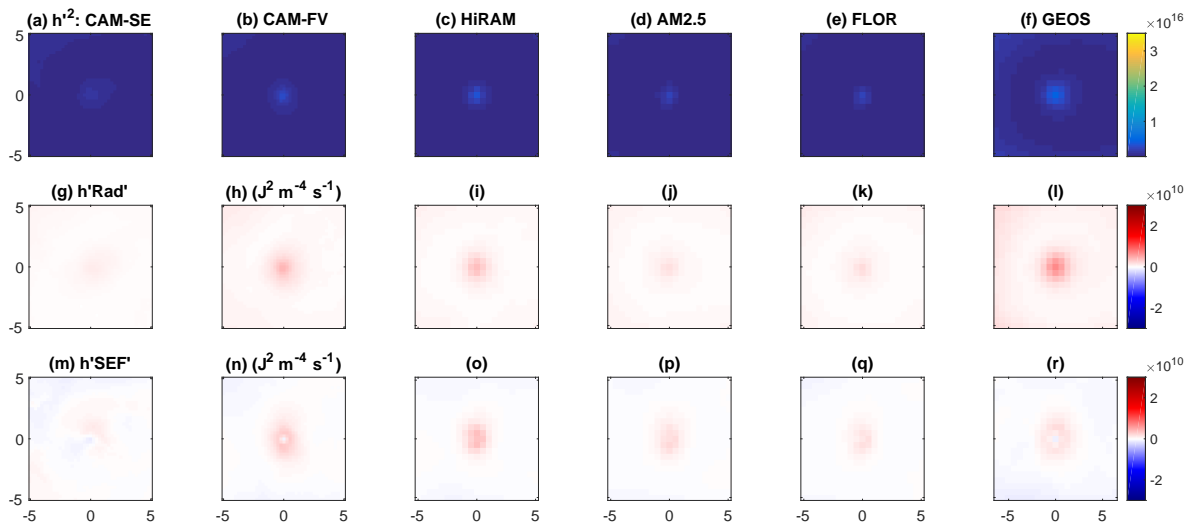
944 FIG. 10. Composite of the box-average MSE variance budget in the CAM-SE (a,g), CAM-FV (b,h), HiRAM
 945 (c,i), AM2.5 (d,j), FLOR (e,k), and GEOS (f,l) simulations. The first row (a-f) shows, as a function of time
 946 relative to LMI, the composite mean TC intensity (red line, right axis) and the box-average MSE variance (blue
 947 line, left axis), scaled by 10^{14} . The second row (g-l) shows, as a function of time relative to LMI, the surface
 948 flux (green line), longwave (blue line), shortwave (red line), and advective (pink line) feedbacks. The composite
 949 is over all TCs that have a LMI in the upper quartile of the LMI distribution.



950 FIG. 11. Panel (a) shows the composite of the box-average surface flux (asterisks) and longwave radiative
 951 feedback (open circles) at 48 hours prior to LMI for each model as a function of that models TC intensity. Panel
 952 (b) shows the ratio of the composite box-average surface flux and radiative feedbacks for each model. Simulated
 953 TC intensity is defined as the average LMI of all TCs that have LMI in the upper quartile of the LMI distribution.
 954 In all panels, the models are CAM-SE (red), CAM-FV (yellow), HiRAM (blue), AM2.5 (purple), FLOR (green)
 955 and GEOS (black). The composite is over all TCs that have a LMI in the upper quartile of the LMI distribution.



956 FIG. 12. Composite of MSE (Jm^{-2} ; a-f), column radiative flux convergence (g-l) and surface fluxes (m-r) as a
 957 function of latitude and longitude relative to the TC center in the $24\text{-}27 \text{ ms}^{-1}$ intensity bin, in CAM-SE (a,g,m),
 958 CAM-FV (b,h,n), HiRAM (c,i,o), AM2.5 (d,j,p), FLOR (e,k,q), and GEOS (f,l,r).



959 FIG. 13. Composite of MSE variance ($J^2 m^{-4}$; a-f), radiative (g-l) and surface flux feedbacks (m-r) as a
 960 function of latitude and longitude relative to the TC center in the $15-18 \text{ ms}^{-1}$ intensity bin, in CAM-SE (a,g,m),
 961 CAM-FV (b,h,n), HiRAM (c,i,o), AM2.5 (d,j,p), FLOR (e,k,q), and GEOS (f,l,r).

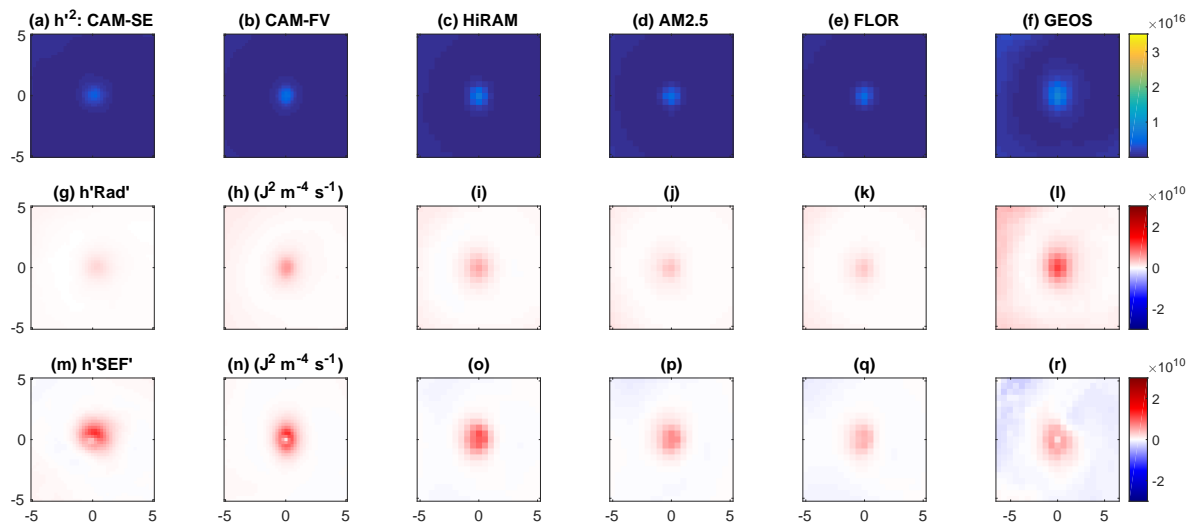


FIG. 14. As in Fig. 13 but for the $24\text{-}27\text{ ms}^{-1}$ intensity bin.

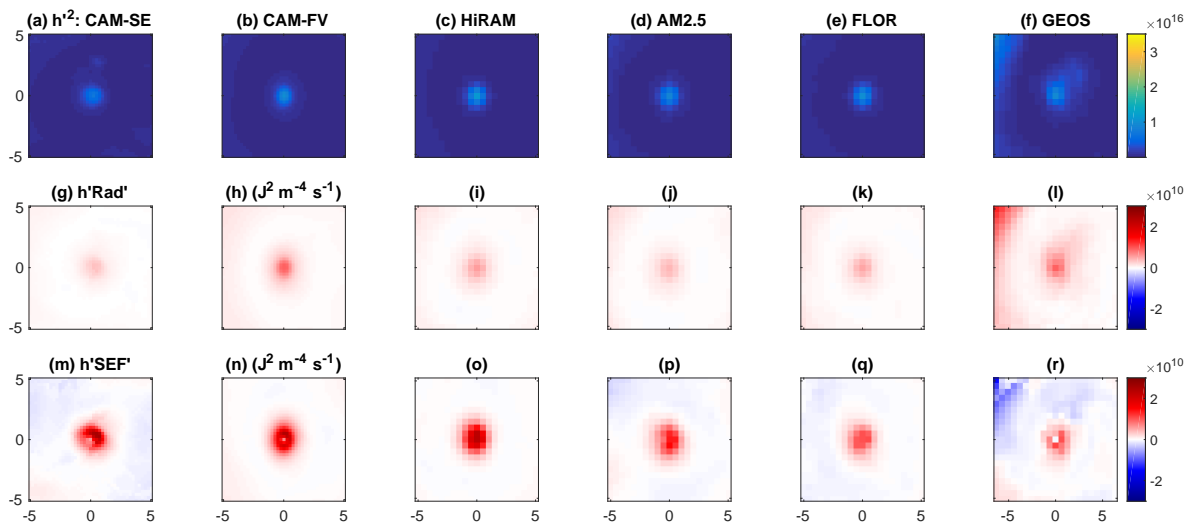
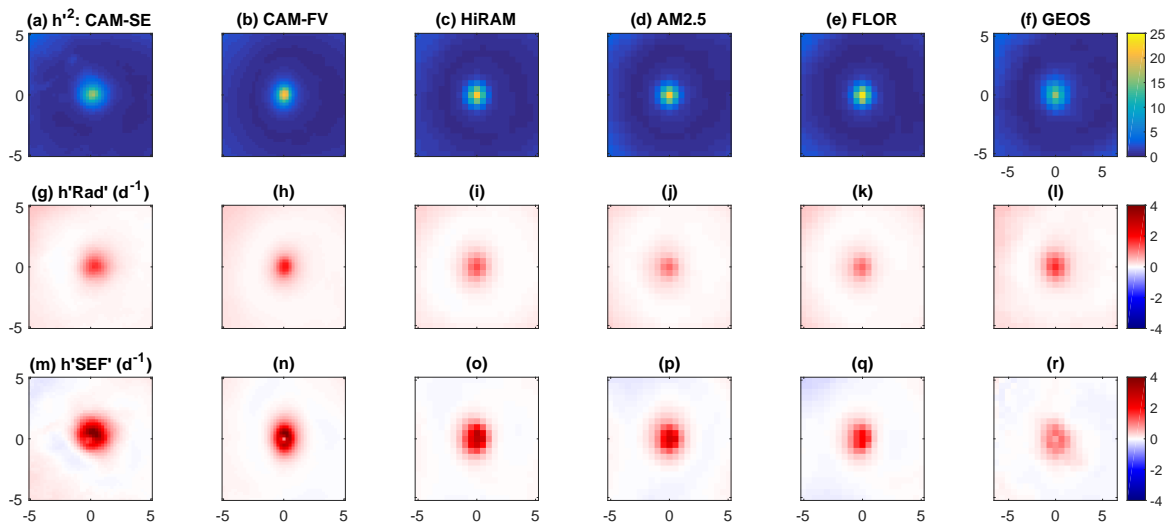
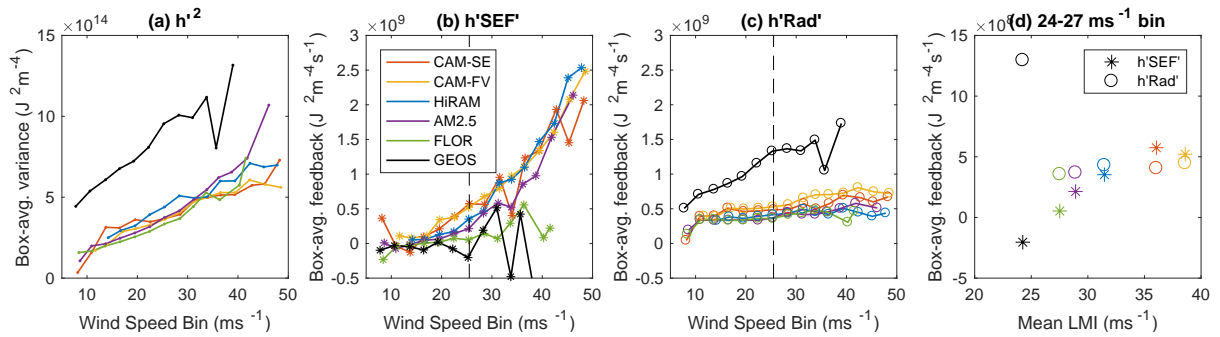


FIG. 15. As in Fig. 13 but for the 33-35 ms^{-1} intensity bin.



962 FIG. 16. Composite of normalized MSE variance (a-f), radiative (g-l) and surface flux feedbacks (m-r) as a
 963 function of latitude and longitude relative to the TC center in the $24\text{-}27\text{ ms}^{-1}$ intensity bin, in CAM-SE (a,g,m),
 964 CAM-FV (b,h,n), HiRAM (c,i,o), AM2.5 (d,j,p), FLOR (e,k,q), and GEOS (f,l,r).



965 FIG. 17. Box-average MSE variance (a) and surface flux (b) and radiative (c) feedback terms in the MSE
 966 variance budget composited over intensity bins. The x-axis indicates the mean wind speed in each bin, for
 967 each model. Panel (c) shows the box-average surface flux (asterisk) and radiative (open circle) feedback terms
 968 composited over the 24-27 ms⁻¹ bin (indicated by the dashed line in (b) and (c)) for each model, as a function
 969 of the mean LMI of simulated TCs in that model.